Mixed Convection from an Isothermal Smooth Plate

Aubrey G. Jaffer and Martin S. Jaffer
e-mail: agj@alum.mit.edu

Abstract

This investigation derives formulas to predict the mixed convection heat transfer of a flat smooth surface having a convex perimeter in a Newtonian fluid with a steady forced flow parallel to that surface.

The present theory was tested with 574 heat transfer measurements in 101 data-sets at 14 orientations from 3 peer-reviewed studies, a Sandia National Laboratories technical report, and the present apparatus. Compared with the present theory, the root-mean-squared relative error values of the 101 data-sets span 0.8% through 5.1%.

This research did not receive any specific grant from funding agencies in the public, commercial, or not-for-profit sectors.

Table of Contents

1. Introduction

Natural convection is the flow caused by nonuniform density in a fluid under the influence of gravity. Forced convection is the heat or solute transfer to or from a surface induced by forced fluid flow parallel to that surface. Mixed convection is the heat or solute transfer when both processes are operating simultaneously. Natural and forced convection are fundamental processes whose combination has applications from engineering to geophysics.

Two modes of forced fluid flow along a (flat) surface are laminar flow and turbulent flow. Flow along flat, smooth plates gradually transitions from laminar to turbulent in a continuous boundary-layer[1] (Lienhard [1]).

Forced convection fluid flow is parallel to the surface. In natural convection the temperature difference between the fluid and surface creates an upward or downward fluid flow, which is not necessarily parallel to the surface. Along a vertical plate, "aiding" has natural and forced flows in the same direction; "opposing" flows are in opposite directions.

Natural convection is sensitive to plate inclination, while forced convection is not. Forced convection has different formulas for laminar and turbulent flows, while a single formula governs both laminar and turbulent natural convection (Fujii and Imura [2] Churchill and Chu [3], Jaffer [4]).

There is a symmetry in external natural convection; a cooled plate induces downward flow instead of upward flow. Flow from a cooled upper face is the mirror image of flow from a heated lower face. Flow from a cooled lower face is the mirror image of flow from a heated upper face.

The rest of this investigation assumes a surface warmer than the fluid.

1.1 Fluid Mechanics.

In engineering, heat transfer rates for both natural and forced convection are expressed using the average surface conductance $\overline{h}$ with units $\mathrm{W}/(\mathrm{m}^2 \cdot \mathrm{K})$.

In fluid mechanics, the convective heat transfer rate is represented by the dimensionless average Nusselt number ($\overline{Nu} \equiv \overline{h}\, L/k$), where k is the fluid's thermal conductivity with units $\mathrm{W}/(\mathrm{m} \cdot \mathrm{K})$, and L is the system's characteristic length (m).

The Reynolds number Re is dimensionless and proportional to fluid velocity. The Rayleigh number Ra is the impetus for fluid flow due to gravity acting on density differences caused by temperature (or diffusion). A fluid's Prandtl number Pr is its momentum diffusivity per thermal diffusivity ratio. The system's characteristic length L scales $\overline{Nu}$ and Re; Ra is scaled by L^3; $\overline{h}$ and Pr are independent of L.

1.2 Combining Transfer Processes.

Formula (1) is an unnamed form for combining functions which appears frequently in heat transfer formulas:

$$F^p = F_1^p + F_2^p \tag{1}$$

Churchill and Usagi [5] stated that such formulas are "remarkably successful in correlating rates of transfer for processes which vary uniformly between these limiting cases." Convection transfers heat (or solute) between the plate and the fluid.

1.3 The ℓ^p-norm.

When $F_1 \geq 0$ and $F_2 \geq 0$, taking the pth root of both sides of Equation (1) yields a vector-space functional form known as the ℓ^p-norm, which is notated $\|F_1\ ,\ F_2\|_p$:

$$\|F_1\ ,\ F_2\|_p \equiv [\ |F_1|^p + |F_2|^p]^{1/p} \tag{2}$$

Norms generalize the notion of distance. Formally, a vector-space norm obeys the triangle inequality: $\|F_1, F_2\|_p \leq |F_1| + |F_2|$, which holds only for $p \geq 1$. However, $p < 1$ is also useful.

When $p > 1$, the processes modeled by F_1 and F_2 compete and $\|F_1, F_2\|_p \geq \max(|F_1|, |F_2|)$; the most competitive case is $\|F_1, F_2\|_{+\infty} \equiv \max(|F_1|, |F_2|)$. The ℓ^2-norm is equivalent to root-sum-squared; it models perpendicular competitive processes.

The ℓ^1-norm models independent processes; $\|F_1, F_2\|_1 \equiv |F_1| + |F_2|$.

When $0 < p < 1$, the processes cooperate and $\|F_1, F_2\|_p \geq |F_1| + |F_2|$. Cooperation between conduction and flow-induced heat transfer occurs in natural convection.

[1] Schlichting [6] describes a boundary-layer: "In that thin layer the velocity of the fluid increases from zero at the wall (no slip) to its full value which corresponds to external frictionless flow."

When $p < 0$, $\|F_1, F_2\|_p \leq \min(|F_1|, |F_2|)$, with the transition sharpness controlled by p; the extreme case is $\|F_1, F_2\|_{-\infty} \equiv \min(|F_1|, |F_2|)$. Negative p can model a single flow through serial processes; the most restrictive process exerts the most control of the flow.

1.4 **Disks.** The primary goal of this investigation is to predict mixed convective heat transfer from a flat surface with a convex perimeter. Any apparatus designed to measure mixed convection from a single flat surface has parasitic (undesired) heat transfers; in the case of laminar mixed convection, these are significant.

Most wind-tunnels operate only at a few airspeeds; airspeeds must be larger than 10 m/s in order to use a hot-wire anemometer to accurately characterize the free-stream turbulence of the airflow. The present open-intake apparatus operates at wind-speeds less than 4.5 m/s.

Without being able to measure the free-stream turbulence, the best option for assuring that forced convection is laminar is to test at small Reynolds numbers. This can be accomplished by changing to a fluid with higher viscosity or by reducing the test surface's characteristic length.

The approach taken by Kobus and Wedekind [7] and this investigation is to measure heat transfer from thermistor disks less than 20 mm in diameter. Thermal insulation is ineffective at such a small scale without its bulk significantly altering fluid flow. Thus, heat transfer of the rim and both sides are measured together.

An approximate whole-disk convection model is developed (and presented) by this investigation to test heat transfer from disks whose thickness to diameter ratio is less than 0.12.

1.5 **Turbulent Convection.** Measuring turbulent convection requires larger Re values than those which produce laminar convection. A 0.305 m square plate is being fabricated to perform such measurements.

2. Prior Works

Most published studies of mixed convection investigate laminar flow. The mixture of laminar and turbulent flows is turbulent. Thus, the natural and forced components of mixed convection must both be laminar if their mixture is to be laminar.

2.1 **Laminar Flow.** Building on the Blasius boundary-layer model of laminar flow (Schlichting [6]), these laminar studies analyze boundary-layer local properties. But streamlines images from Fujii and Imura [2] and Kitamura, Mitsuishi, Suzuki, and Kimura [8] show natural convection's boundary layer detaching from the center of an upward-facing plate. Streamlines images from Fujii and Imura [2] and Aihara, Yamada, and Endö [9] (see Figure 3) show that the downward-facing boundary layer is split in half. Thus, these prior studies of local laminar convection are limited to a small subset of mixed convection use cases.

Lin, Yu, and Chen [10] presents formulas for local mixed convection for aiding forced flow and opposing forced flow along a vertical plate, and aiding and opposing flow along a downward facing plate. Absent are horizontal forced flow along a vertical plate, and forced flow along an upward facing plate.

The local Nusselt number graphs in Lin et al. [10] show many points from numerical simulations of aiding flow over a wide range of Pr, but only four closely spaced opposing flow points. The opposing flow curve ends abruptly because their formula, $\sqrt[4]{1 - X^4}$, has no physical interpretation when $X > 1$.

Ramachandran, Armaly, and Chen [11] measured local laminar aiding and opposing convection heat transfer along a vertical plate. As with Lin et al. [10], opposing flow was tested only at low Re values.

Kobus and Wedekind [7] measured laminar mixed convection heat transfer along a vertical disk. The measurements from graphs in the article were captured by measuring the distance from each point to its graph's axes, then scaling to the graph's units using the "Engauge" software (version 12.1).

2.2 **Laminar Turbulent Transition.** Intended for solar central power applications, Siebers, Schwind, and Moffat [12] measured mixed convection heat transfer from a 3 m square vertical surface at temperatures between 40 C and 600 C in horizontal flow at speeds between 1.3 m/s and 6.2 m/s. Although the surface was located in the vertical wall of a wind-tunnel, the pressure drop across it was negligible. The measurements were input from the table in [12] appendix E.

Wang [13] reported local measurements of a horizontal flat plate in a wind tunnel at wind speeds and with temperature differences sufficient to test both laminar and turbulent flows. Unfortunately, the plate was one of the test chamber walls. The downward facing natural convection flow described earlier would not form because fluid could not rise upon reaching the plate edge. The horizontal flows of the upward facing configuration were obstructed by the test chamber walls.

3. Data-Sets and Evaluation

Table 1 Disk natural convection data-sets

Source	d	t/d	θ	ϕ	$Ra_d \geq$	$Ra_d \leq$	$Re_d \geq$	$Re_d \leq$	$\pm$	#
[7]	15.29 mm	0.058	0.0°		7.3×10^2	5.5×10^3	0	0	12%	21
[7]	19.99 mm	0.069	0.0°		2.1×10^3	1.2×10^4	0	0	12%	8
[7]	10.52 mm	0.097	0.0°		1.4×10^2	1.7×10^3	0	0	12%	17
[7]	7.43 mm	0.155	0.0°		6.6×10^1	5.9×10^2	0	0	12%	17
[14]	15.47 mm	0.063	30.0°		5.3×10^3	2.5×10^4	0	0	12%	16
[14]	19.99 mm	0.069	30.0°		8.9×10^3	2.7×10^4	0	0	12%	9
[14]	10.48 mm	0.090	30.0°		1.2×10^3	7.8×10^3	0	0	12%	17
[14]	7.43 mm	0.155	30.0°		4.8×10^2	2.6×10^3	0	0	12%	13
[14]	5.20 mm	0.163	30.0°		1.5×10^2	8.5×10^2	0	0	12%	11
[14]	15.47 mm	0.063	60.0°		4.6×10^3	2.6×10^4	0	0	12%	14
[14]	19.99 mm	0.069	60.0°		8.9×10^3	2.6×10^4	0	0	12%	10
[14]	10.48 mm	0.090	60.0°		1.1×10^3	7.0×10^3	0	0	12%	15
[14]	7.43 mm	0.155	60.0°		9.5×10^2	2.6×10^3	0	0	12%	14
[14]	5.20 mm	0.163	60.0°		1.3×10^2	8.9×10^2	0	0	12%	12
[15]	15.47 mm	0.063	90.0°		9.8×10^3	2.5×10^4	0	0	12%	3
[15]	19.99 mm	0.069	90.0°		8.5×10^3	5.1×10^4	0	0	12%	8
[15]	10.48 mm	0.090	90.0°		3.4×10^3	6.3×10^3	0	0	12%	5
[15]	7.43 mm	0.155	90.0°		5.6×10^2	2.3×10^3	0	0	12%	10
[15]	5.20 mm	0.163	90.0°		1.2×10^2	6.9×10^2	0	0	12%	6

The present apparatus combines an open intake wind-tunnel, software phase-locked loop fan control, and, for laminar measurements, a thickness $t = 1$ mm, diameter $d = 12$ mm positive temperature coefficient thermistor disk held in place by a fixture contacting the disk at four points. Tests were conducted in air at temperatures between 18 C and 21 C with disk temperatures between 36 C and 60 C and flows $91 < Re_d < 2100$. The disk apparatus and measurement methodology are described in detail in Section 13.

For turbulent measurements, the disk and its fixture were replaced with a 0.305 m square plate centered in the test chamber by a six wire suspension. This apparatus measured average mixed convection in air with $2300 < Re < 93000$. An appendix of Jaffer and Jaffer [16] describes the apparatus and measurement methodology (with different 0.305 m square plates).

In both configurations the wind-tunnel chassis (1.3 m × 0.61 m × 0.65 m) was small enough to allow its positioning in horizontal, vertical, and inclined orientations. $0° \leq \psi \leq 180°$ is the forced flow angle from zenith ($\psi = 0°$ is upward flow); θ is the plate angle from vertical ($\theta = +90°$ is level with face upward).

Table 2 Disk Laminar mixed convection data-sets

Source	d	t/d	θ	ϕ	$Ra_d \geq$	$Ra_d \leq$	$Re_d \geq$	$Re_d \leq$	$\pm$	#
[7]	15.27 mm	0.062	0.00°	90.00°	4.9×10^3	4.9×10^3	1.1×10^3	2.5×10^4	12%	16
[7]	19.99 mm	0.069	0.00°	0.00°	1.1×10^4	1.1×10^4	3.4×10^0	1.0×10^3	12%	24
[7]	7.43 mm	0.155	0.00°	0.00°	5.6×10^2	5.6×10^2	2.0×10^0	7.6×10^2	12%	24
present	11.96 mm	0.092	0.00°	0.00°	2.8×10^3	5.3×10^3	1.4×10^2	2.0×10^3	5%	35
present	11.96 mm	0.092	0.00°	180.00°	2.5×10^3	5.3×10^3	9.2×10^1	2.0×10^3	5%	59
present	11.96 mm	0.092	0.00°	173.30°	2.6×10^3	5.3×10^3	9.2×10^1	2.0×10^3	5%	58
present	11.96 mm	0.092	0.00°	96.80°	3.5×10^3	5.9×10^3	1.3×10^2	2.0×10^3	3%	34
present	11.96 mm	0.092	0.00°	90.00°	3.4×10^3	5.8×10^3	1.3×10^2	2.0×10^3	3%	34
present	11.96 mm	0.092	0.00°	7.71°	2.4×10^3	5.2×10^3	8.9×10^1	2.0×10^3	5%	44
present	11.96 mm	0.092	90.00°	90.00°	3.4×10^3	5.8×10^3	1.3×10^2	2.0×10^3	3%	34
present	11.96 mm	0.092	7.40°	90.00°	3.4×10^3	5.9×10^3	1.4×10^2	2.0×10^3	3%	34
present	11.96 mm	0.092	82.60°	90.00°	3.0×10^3	5.8×10^3	1.3×10^2	2.1×10^3	3%	35
present	11.96 mm	0.092	6.65°	173.30°	2.5×10^3	5.3×10^3	9.1×10^1	2.0×10^3	5%	58
present	11.96 mm	0.092	81.50°	98.50°	3.0×10^3	5.8×10^3	1.3×10^2	2.1×10^3	3%	35
present	11.96 mm	0.092	7.71°	7.71°	2.4×10^3	5.2×10^3	8.9×10^1	2.0×10^3	5%	43

Table 3 Laminar–turbulent transitional mixed convection

Source	Dimensions	θ	ϕ	$Ra \geq$	$Ra \leq$	$Re \geq$	$Re \leq$	$\pm$	#
[12]	2.95 m × 3.02 m	0.0°	90.0°	5.7×10^{10}	2.2×10^{11}	9.0×10^{4}	1.1×10^{6}	6-10%	46

3.1 **Natural Convection Data-sets.** Table 1 lists the Kobus and Wedekind natural convection data-sets. Results from disks whose thickness to diameter ratio $t/d > 0.12$ are not included in Section 9.

3.2 **Mixed Convection Data-sets.** Table 2 lists the laminar mixed convection data-sets. Table 3 lists the mixed convection data-set with Re values spanning laminar and turbulent forced flows.

3.3 **Not Empirical.** Empirical theories derive their coefficients from measurements, inheriting the uncertainties from those measurements. Theories developed from first principles derive their coefficients mathematically. For example, Incropera, DeWitt, Bergman, and Lavine [17] gives the thermal conductance of one face of a diameter D disk into a stationary, uniform medium having thermal conductivity k as $8\,k/[\pi\,D]$ (units $\mathrm{W}/(\mathrm{m}^2 \cdot \mathrm{K})$).

The present theory predicting mixed convective heat transfer from a single flat surface derives from first principles; it is not empirical. Each formula is tied to aspects of the plate geometry and orientation, fluid, and flow.

The present whole-disk theory is less certain; it is crafted for laminar flow and a disk whose thickness to diameter ratio is less than 0.12.

3.4 **RMS Relative Error.** Root-mean-squared (RMS) relative error (RMSRE) provides an objective, quantitative evaluation of experimental data versus theory. It gauges the fit of measurements $g(Re_j)$ to function $f(Re_j)$, giving each of the n samples equal weight in Formula (3). Along with presenting RMSRE, charts in the present work split RMSRE into the bias and scatter components defined in Formula (4). The root-sum-squared of bias and scatter is RMSRE.

$$\mathrm{RMSRE} = \sqrt{\frac{1}{n}\sum_{j=1}^{n}\left|\frac{g(Re_j)}{f(Re_j)} - 1\right|^2} \tag{3}$$

$$\mathrm{bias} = \frac{1}{n}\sum_{j=1}^{n}\left\{\frac{g(Re_j)}{f(Re_j)} - 1\right\} \qquad \mathrm{scatter} = \sqrt{\frac{1}{n}\sum_{j=1}^{n}\left|\frac{g(Re_j)}{f(Re_j)} - 1 - \mathrm{bias}\right|^2} \tag{4}$$

4. Natural Convection

Jaffer [4] derived a natural convection formula for external flat plates (with convex perimeter) in any orientation from its analyses of horizontal and vertical plates. This investigation uses the same approach.

Figures 1, 2, and 3 show the induced fluid flows around heated vertical and horizontal surfaces. Horizontal flow in Figure 2 is radial, but not radial in Figure 3. Horizontal flow is nearly absent at the elevation of the dashed line in Figure 2.

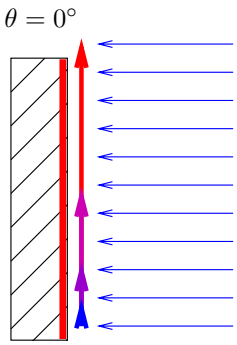

Figure 1 Vertical plate

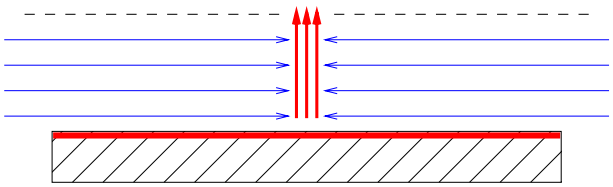

Figure 2 Flow above a heated plate; $\theta = -90°$

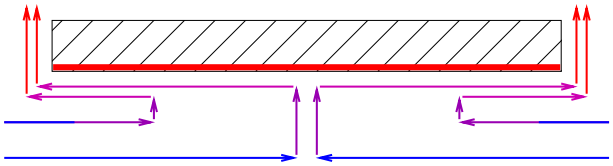

Figure 3 Flow below a heated plate; $\theta = +90°$

An important aspect of all three flow topologies is that fluid is pulled horizontally before being heated by the plate. Pulling horizontally expends less energy than pulling vertically because the latter does work against the gravitational force. Inadequate horizontal clearance around a plate can obstruct flow and reduce convection and heat transfer.

From thermodynamic constraints, Jaffer [4] derives generalized natural convection Formula (5) with the parameters specified in Table 4:

$$\overline{Nu} = \left\| Nu_0 \left[1 - C\right],\ \sqrt[2+E]{\left[C\,D\,Nu_0\right]^{3+E}\,\frac{2}{B}\,Ra} \right\|_p \tag{5}$$

$$\Xi = \left\| 1\ ,\ \frac{0.5}{Pr} \right\|_{\sqrt{1/3}} \qquad Nu_0^* = \frac{2}{\pi} \approx 0.637 \qquad Nu_0' = \frac{2^4}{\sqrt[4]{2}\,\pi^2} \approx 1.363 \tag{6}$$

Table 4 Natural convection parameters

Face	θ	L	$\overline{Nu}$	Nu_0	Ra	E	B	C	D	p
up	$-90°$	L^*	$\overline{Nu^*}$	Nu_0^*	Ra^*	1	2	$1/\sqrt{8}$	1	1/2
vertical	$0°$	L'	$\overline{Nu'}$	Nu_0'	Ra'/Ξ	1	1/2	1/2	1/4	1/2
down	$+90°$	L_R	$\overline{Nu_R}$	$Nu_0'/2$	Ra_R/Ξ	3	4	1/2	2	1

- θ is the angle of the plate from vertical; $\theta = +90°$ is face down;
- L is the characteristic length of a flat plate with convex perimeter:
  - face up ($\theta = -90°$) L^* is the area-to-perimeter ratio;
    - For a $Y \times Z$ rectangle, $L^* = Y\,Z/[2\,Y + 2\,Z]$.
    - For a diameter D disk, $L^* = D/4$.
  - vertical ($\theta = 0°$) L' is the harmonic mean of the perimeter vertical spans;
    - Given a convex vertical plate with maximum width W whose vertical span at horizontal offset w is $H(w)$:

$$L' = W \Big/ \int_0^W \frac{1}{H(w)}\,\mathrm{d}w \tag{7}$$

    * For a level height H rectangle, $L' = H$.
    * For a diameter D disk, $L' = 2\,D/\pi$.

— face down ($\theta = +90°$) L_R is the harmonic mean of the perimeter distances to that bisector which is perpendicular to the shortest bisector;

    * Given a flat surface with convex perimeter defined by functions $H_+(w) > 0$ and $H_-(w) < 0$ within the range $0 < w < W$ along the equal-area bisector which is perpendicular to the shortest equal-area bisector:

$$L_R = 4\,W \Bigg/ \int_0^W \left[\frac{1}{|H_+(w)|} + \frac{1}{|H_-(w)|}\right] \mathrm{d}w \tag{8}$$

    * For a $Y \times Z$ rectangle, $L_R = \min(Y, Z)/2$.
    * For a diameter D disk, $L_R = D/\pi$.

- Nu_0 is the conduction into the fluid when not moving (static);
- Ra' is computed with vertical L'; $Ra^* = Ra'\,[L^*/L']^3$; $Ra_R = Ra'\,[L_R/L']^3$.
  Pr does not affect upward-facing heat transfer because the heated fluid flows directly upward, as does conducted heat. When heated fluid must flow along vertical and downward-facing plates, its heat transfer potential is reduced by dividing Ra by Ξ from Formula (6).
- E is the count of 90° changes in direction of fluid flow;
- B is the sum of the mean lengths of flows parallel to the plate divided by L;
- C is the plate area fraction responsible for flow induced heat transfer;
- D is the effective length of heat transfer contact with the plate divided by L;
- The ℓ^p-norm combines the static conduction and induced convective heat flows.

4.1 **Surface Conductance Formulas.** Because the characteristic lengths scaling $\overline{Nu^*}$, $\overline{Nu'}$, and $\overline{Nu_R}$ can be different, combining them works in terms of $\overline{h^*}$, $\overline{h'}$, and $\overline{h_R}$ (or $\overline{U^*} = A\,\overline{h^*}$, $\overline{U'} = A\,\overline{h'}$, and $\overline{U_R} = A\,\overline{h_R}$):

$$\overline{h^*}(Ra^*) = \frac{k}{L^*}\left\|Nu_0^*\left[1 - \frac{1}{\sqrt{8}}\right]\ ,\ \frac{{Nu_0^*}^{4/3}}{4}\sqrt[3]{Ra^*}\right\|_{1/2} \approx \frac{k}{L^*}\left\|0.411\ ,\ 0.137\sqrt[3]{Ra^*}\right\|_{1/2} \tag{9}$$

$$\overline{h'}(Ra') = \frac{k}{L'}\left\|\frac{Nu_0'}{2}\ ,\ \frac{{Nu_0'}^{4/3}}{8\sqrt[3]{2}}\sqrt[3]{\frac{Ra'}{\Xi}}\right\|_{1/2} \approx \frac{k}{L'}\left\|0.682\ ,\ 0.150\sqrt[3]{\frac{Ra'}{\Xi}}\right\|_{1/2} \tag{10}$$

$$\overline{h_R}(Ra_R) = \frac{k}{L_R}\left\|\frac{Nu_0'}{4}\ ,\ \frac{{Nu_0'}^{6/5}}{2^{7/5}}\sqrt[5]{\frac{Ra_R}{\Xi}}\right\|_1 \approx \frac{k}{L_R}\left[0.341 + 0.550\sqrt[5]{\frac{Ra_R}{\Xi}}\right] \tag{11}$$

4.2 **Natural Convection From an Inclined Plate.** Ra is proportional to gravitational acceleration. Following the approach of Fujii and Imura [2], the Ra argument to $\overline{h'}(Ra) \equiv k\,\overline{Nu'}(Ra)/L'$ is scaled by $|\cos\theta|$, modeling the reduced convection of a tilted plate as a reduction in gravitational acceleration. Similarly, the Ra arguments to $\overline{h^*}$ and $\overline{h_R}$ are scaled by $|\sin\theta|$. An unobstructed plate induces a single steady-state mode of natural convection (face up, down, or vertical). The instances of max() in Formula (12) choose the largest surface conductance among these modes.

$$\overline{h} = \begin{cases} \max\left(\overline{h'}(|\cos\theta|\,Ra'/\Xi),\ \overline{h^*}(|\sin\theta|\,Ra^*)\right) & \sin\theta < 0 \\ \max\left(\overline{h'}(|\cos\theta|\,Ra'/\Xi),\ \overline{h_R}\,(|\sin\theta|\,Ra_R/\Xi)\right) & \sin\theta \geq 0 \end{cases} \tag{12}$$

In reality, the θ transition is more gradual using the ℓ^{16}-norm in Formula (13):

$$\overline{h} = \begin{cases} \left\|\overline{h'}(|\cos\theta|\,Ra'/\Xi),\ \overline{h^*}(|\sin\theta|\,Ra^*)\right\|_{16} & \sin\theta < 0 \\ \left\|\overline{h'}(|\cos\theta|\,Ra'/\Xi),\ \overline{h_R}\,(|\sin\theta|\,Ra_R/\Xi)\right\|_{16} & \sin\theta \geq 0 \end{cases} \tag{13}$$

4.3 **Disk Natural Convection.** As with the present thermistor disk apparatus, the apparatuses used by Kobus and Wedekind [7, 15, 14] measured total heat transfer of an uninsulated disk.

This section analyzes the simultaneous convective heat transfer of the rim and both sides of a disk by accounting for each component of its surface and flows. A flow which touches more than one surface element may experience "reuptake", a reduction in total heat transfer due to contact with already heated fluid. Reuptake terms will be subtracted from the total potential heat transfer of the whole disk.

Each Rayleigh number (Ra) is computed using the characteristic length L with matching subscripts and superscripts. Trigonometric Ra coefficients are included in anticipation of the inclined disk analysis.

4.4 **Vertical Disk.** The heat transfer of each vertical face (of area $A_\bullet = \pi\, d^2/4$) is:

$$\overline{U'} = \frac{k\, A_\bullet}{L'}\, \overline{Nu'}(|\cos\theta|\, Ra') = \frac{\pi^2\, d\, k}{8}\, \overline{Nu'}(|\cos\theta|\, Ra') \qquad L' = \frac{2\, d}{\pi} \tag{14}$$

Fluid at the bottom of a wide rim flows in the vertical plane. Fluid near the bottom of a thin rim behaves as fluid near a downward-facing plate with 1/4 of the rim's area $A_\circ = \pi\, t\, d$ and $L_\cup = t/2$:

$$\overline{U_\cup} = \frac{k\, A_\circ}{4\, L_\cup}\, \overline{Nu_R}(|\cos\theta|\, Ra_\cup) = \frac{\pi\, k\, d}{2}\, \overline{Nu_R}(|\cos\theta|\, Ra_\cup) \tag{15}$$

This fluid heated by the bottom rises near the flat disk faces, reducing their convective heat transfers. Part of $\overline{U_\cup}$ will be deducted as reuptake.

Fluid at the top of a thin rim flows inward from above the flat faces; it is modeled by increasing the effective $\overline{U'}$ area by 1/4 of the rim area. However, the fluid above the flat faces is already heated. The total heat transfer is reduced by the top 1/4 of the thin rim acting as an upward-facing plate with $L^*_\cap = A_\circ/[8\, t + 2\, \pi\, d]$:

$$\overline{U_\cap} = \frac{k\, A_\circ}{4\, L^*_\cap}\, \overline{Nu^*}(|\cos\theta|\, Ra^*_\cap) = k\, \left[2\, t + \frac{\pi\, d}{2}\right]\, \overline{Nu^*}(|\cos\theta|\, Ra^*_\cap) \tag{16}$$

The remaining left and right rim quarters behave as vertical plates with characteristic length $L'_| = \pi\, d/4$ and natural convective conductance (each):

$$\overline{U_|} = k\, t\, \overline{Nu'}(|\cos\theta|\, Ra'_|)/4 \tag{17}$$

The left and right quarters do not significantly interact with vertical flat faces.

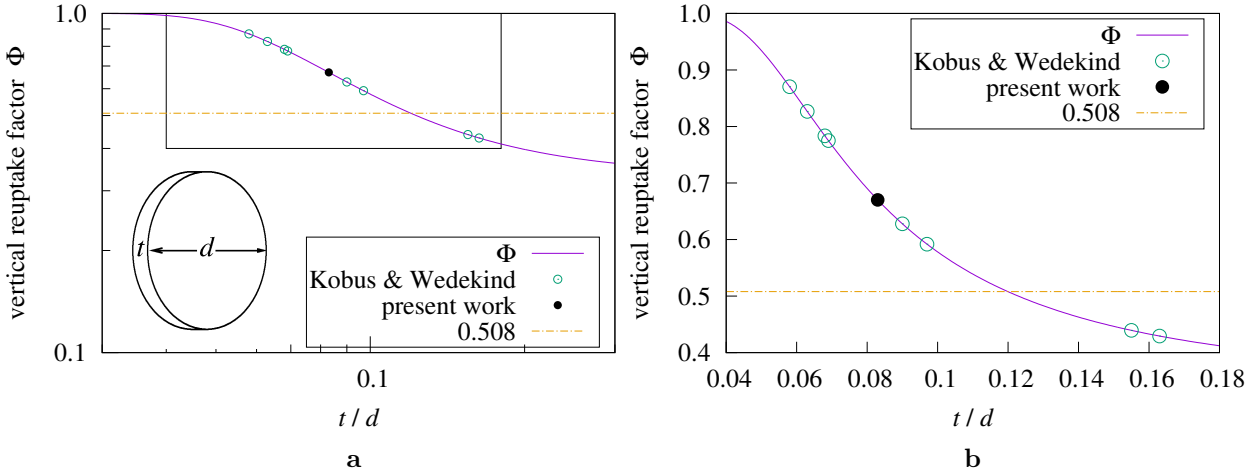

Figure 4 Vertical disk reuptake coefficient (a) curve (b) detail

These rim formulas are for very thin disks. The prior work disk data comes from disks with t/d ratios between 0.058 and 0.163. The reuptake coefficient $1/3 < \Phi < 1$ is introduced in order to stretch the present model to ratios $0 < t/d < 0.12$:

$$\Phi = \exp_3\left(-\exp_3\left(-\left[4\, \pi\, t/d\right]^{-2}\right)\right) \qquad \exp_b(\varpi) \equiv b^{\varpi} \tag{18}$$

Φ is graphed in Figure 4. Circles mark each t/d tested in the present and prior works. Circles below the 0.508 line have $t/d > 0.12$ and are outside the scope of Formula (18).

The negated terms in combined conductance Formula (19) are the reuptake heat transfer reductions described above. The $\cos^4\theta$ and $\cos^8\theta$ coefficients reflect the sensitivity of the top reuptake and bottom reuptake to disk angle.

$$\left[2 + \frac{t}{d}\right] \overline{U'} + 2\,\overline{U_|} + \overline{U_\cup} - \Phi\,\left[\cos^4\theta\,\overline{U_\cap} + \cos^8\theta\,\overline{U_\cup}\right] \tag{19}$$

4.5 **Horizontal Disk.** For the vertical disk, the convective conductance of both flat faces was the same. The horizontal disk upward and downward faces convect differently as $\overline{U^*}$ and $\overline{U_R}$, respectively:

$$\overline{U^*} = \frac{k\,A_\bullet}{L^*}\,\overline{Nu^*}(|\sin\theta|\,Ra^*) = \pi\,d\,k\,\overline{Nu^*}(|\sin\theta|\,Ra^*) \qquad L^* = \frac{d}{4} \tag{20}$$

$$\overline{U_R} = \frac{k\,A_\bullet}{L_R}\,\overline{Nu_R}(|\sin\theta|\,Ra_R) = \frac{\pi^2\,d\,k}{4}\,\overline{Nu_R}(|\sin\theta|\,Ra_R) \qquad L_R = \frac{d}{\pi} \tag{21}$$

Horizontal rim convection $\overline{U_=}$ is modeled as a vertical surface of height t and area $A_\circ$:

$$\overline{U_=} = \frac{k\,A_\circ}{L_=}\,\overline{Nu'}(|\sin\theta|\,Ra') = k\,\pi\,d\,\overline{Nu'}(|\sin\theta|\,Ra') \qquad L_= = t \tag{22}$$

Figure 2 shows that flow is inward above the upper surface; this heated surface will draw fluid heated by the rim as it rises above the upper surface. Fluid heated by the lower face suppresses heat transfer by the rim and upper face. Because downward natural convection $\overline{U_R}$ is less than upward convection $\overline{U^*}$ from the same (horizontal) face area, $\overline{U_R}$ reuptake is nearly complete, leading to the $-\sin^2\theta\,\overline{U_R}$ reuptake term in Formula (23)

Downward natural convection rises along one pair of opposite edges of a square face, leaving the other edges to support vertical convection from the rim. For horizontal disks, the portions appear to be unequal; let shape factor $S_\circ = 2^{-5/4} \approx 0.420$ for the lower face flow, and $1 - S_\circ \approx 0.580$ for the remainder of the rim.

The horizontal disk model scales the top face natural effective area by $1 + 4\,S_\circ\,t/d$, and scales the rim effective area by $1 - S_\circ$:

$$\left[1 + 4\,S_\circ\,\frac{t}{d}\right] \overline{U^*} + [1 - S_\circ]\,\overline{U_=} + \overline{U_R} - \sin^2\theta\,\overline{U_R} \tag{23}$$

In this environment, the stipulation that $t/d < 0.12$ assures that the combination of convection from the rim ($\overline{U_=}$) and lower face ($\overline{U_R}$) does not overwhelm convection from the upper face ($\overline{U^*}$).

4.6 **Inclined Disk.** Competing similarly to $\overline{h}$ Formula (13), the non-reuptake terms of vertical Formula (19) and horizontal Formula (23) combine as the ℓ^{16}-norm in Formula (24).

In splitting the $[t/d]\,\overline{U'}$ term, the upward face gets $[1 - S_\circ]\,[t/d]\,\overline{U'}$, while the lower face gets $S_\circ\,[t/d]\,\overline{U'}$. Yet, for a vertical disk ($\theta = 0°$) Formula (24) matches Formula (19).

At $\theta \approx \pm 45°$, there is an additional reuptake path involving a disk's face and the vertical portion of one side of the rim: $2\,|\sin\theta\,\cos\theta|\,\overline{U_|}$. Each of the other reuptake terms compete with $2\,|\sin\theta\,\cos\theta|\,\overline{U_|}$ as the ℓ^{16}-norm so that this reuptake mode is (practically) exclusive of them.

$$\begin{aligned}\overline{U_N} = &\left\|\left[1 + 4\,S_\circ\,\frac{t}{d}\right]\,\overline{U^*}\;,\;\left[1 + [1 - S_\circ]\,\frac{t}{d}\right]\,\overline{U'} + \overline{U_|} + \frac{\overline{U_\cup}}{2}\right\|_{16} \\ &+ \left\|[1 - S_\circ]\,\overline{U_=} + \overline{U_R}\;,\;\left[1 + S_\circ\,\frac{t}{d}\right]\,\overline{U'} + \overline{U_|} + \frac{\overline{U_\cup}}{2}\right\|_{16} \\ &- \left\|\Phi\left[\cos^4\theta\,\overline{U_\cap} + \cos^8\theta\,\overline{U_\cup}\right]\;,\;2\,|\sin\theta\,\cos\theta|\,\overline{U_|}\right\|_{16} \\ &- \left\|\sin^2\theta\,\overline{U_R}\;,\;2\,|\sin\theta\,\cos\theta|\,\overline{U_|}\right\|_{16}\end{aligned} \tag{24}$$

4.7 **Small Rayleigh Numbers.** With $Ra = 0$ Formulas (9), (10), and (11) predict:

$$\overline{h^*}(0) \approx \frac{k}{L^*}\,0.411 \qquad \overline{h'}(0) \approx \frac{k}{L'}\,0.682 \qquad \overline{h_R}(0) \approx \frac{k}{L_R}\,0.341 \tag{25}$$

Thus, vertical disks at small Ra can have $\overline{U^*} > \overline{U'}$ or $\overline{U_R} > \overline{U'}$, causing $\overline{U_N}$ Formula (24) to predict more heat transfer than it should. To prevent this:

- $\overline{U^*}$ should be forced to 0 when $|\sin^3\theta|\, Ra^* < 1/4$;
- $\overline{U_R}$ and $\overline{U_=}$ should be forced to 0 when $|\sin^3\theta|\, Ra_R < 1/2$.

4.8 **Natural Convection Heat Transfer Measurements.** Kobus and Wedekind [7] measured natural and mixed convection heat transfer from vertical thermistor disks in air. The present theory (line) versus their natural convection measurements (points) are presented in Figure 5.

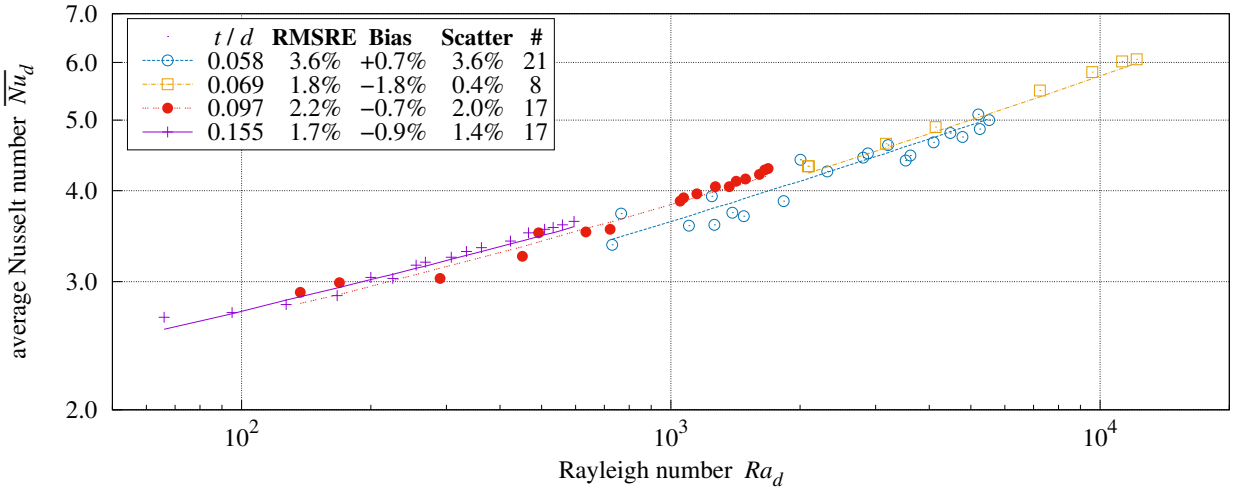

Figure 5 Kobus and Wedekind natural convection heat transfer from vertical disk

Although prior measurements of mixed convection from a horizontal disk are lacking, Kobus and Wedekind [15] measured natural convection from horizontal disks. The present theory versus their measurements are presented in Figure 6.

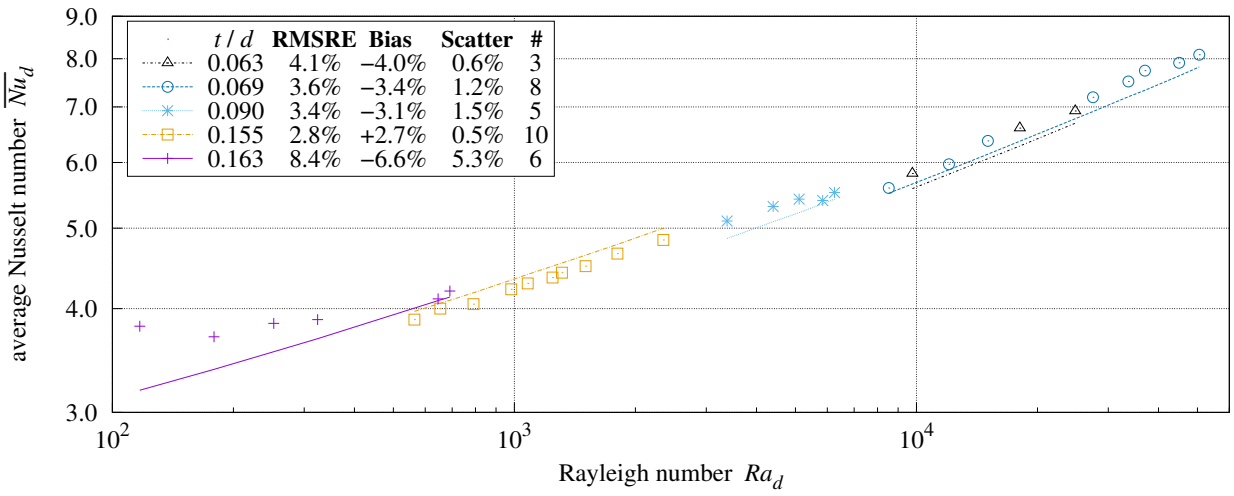

Figure 6 Kobus and Wedekind natural convection heat transfer from horizontal disk

In the case of the 5.20 mm disk with $t/d = 0.163$, the heat transfer from the bottom face and $1 - S_\circ$ of the rim $\overline{U_R} + [1 - S_\circ]\,\overline{U_=}$ exceeds the potential heat transfer from the upper face $[1 + 4\,S_\circ\,t/d]\,\overline{U^*}$. Thus not all of the rising heat is subject to reuptake, leading to 8.7% RMSRE. This is not the case for the 7.43 mm disk with $t/d = 0.155$, although it does not meet the $t/d < 0.12$ stipulation of the present theory.

Kobus and Wedekind [14] measured natural convection from disks inclined at 30° and 60°; the present theory is compared with their measurements in Figures 7 and 8, respectively.

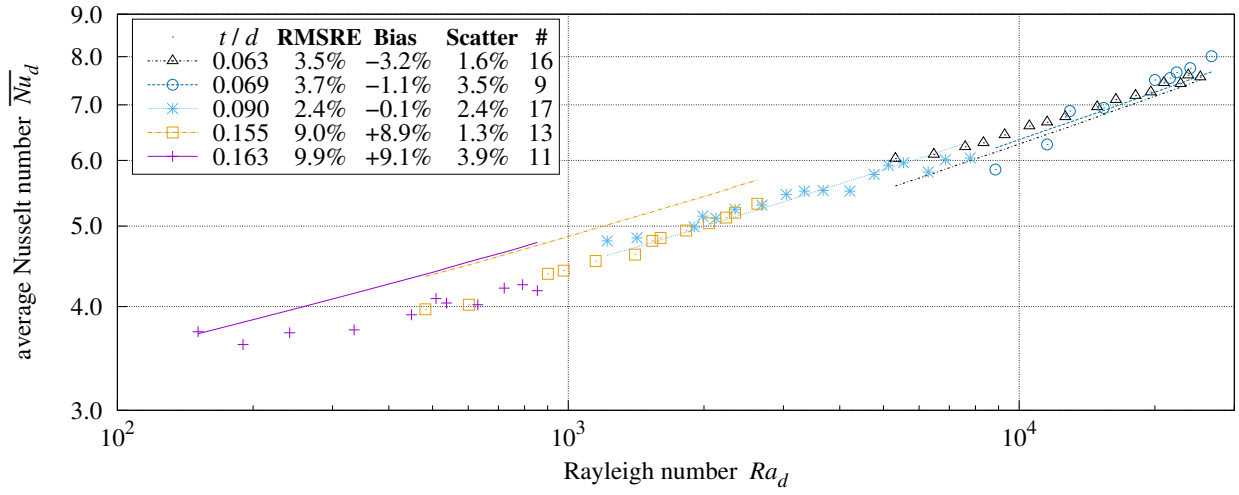

Figure 7 Kobus and Wedekind natural convection heat transfer from 30° angled disk

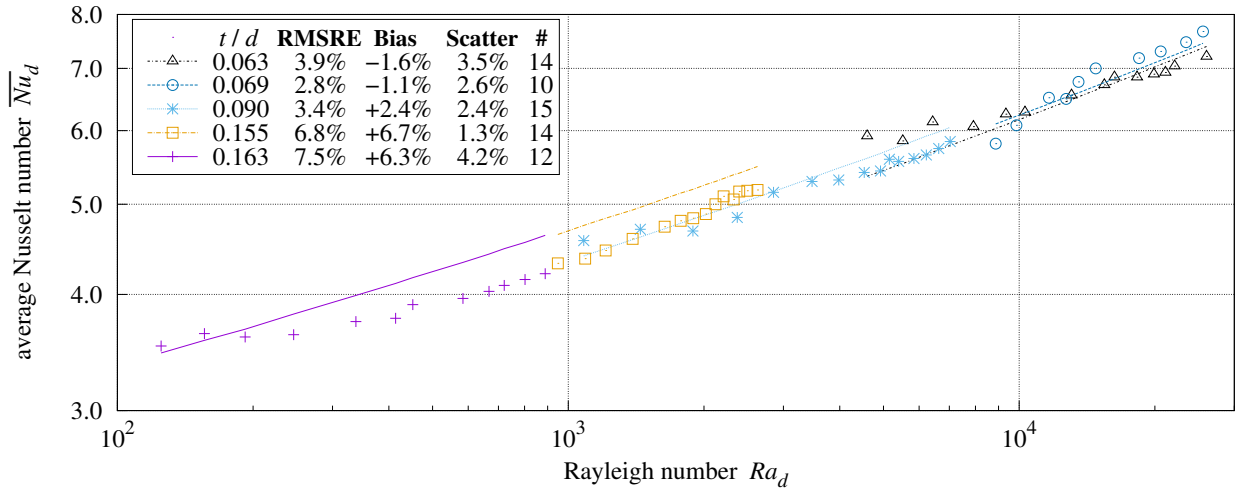

Figure 8 Kobus and Wedekind natural convection heat transfer from 60° angled disk

Excepting the 5.20 mm disk with $t/d = 0.163$ and the 7.43 mm disk with $t/d = 0.155$, the RMSRE values of these Kobus and Wedekind [14] data-sets span 1.8% through 4.1%.

5. Forced Convection

Forced convection $\overline{Nu}$ is the heat transfer caused by forced flow along (and parallel to) a heated plate. The surface conductance $\overline{h_F} \equiv \overline{Nu}\, k/L_F$ grows with Re_F, Pr, and k. Its characteristic length L_F is the same as vertical natural convection's L' Formula (7), the harmonic mean of the perimeter spans in the direction of forced flow; for a diameter D disk, $L_F = L' = 2\,D/\pi$.

5.1 **Laminar Forced Convection.** Jaffer [18] gives the forced convection heat transfer $\overline{Nu_\lambda}$ of laminar forced flow along a smooth, flat plate as:

$$\overline{Nu_\lambda}(Re_F) = \frac{0.664\, Re_F\, Pr^{1/3}}{\sqrt{Re_F} + \sqrt{Re_0}} \qquad Re_0 \approx 600 \tag{26}$$

5.2 **Turbulent Forced Convection.** Jaffer [18] derives the average (not local) surface conductance, $\overline{h_F} \equiv \overline{Nu_\tau}\, k/L_F$, of turbulent flow along a smooth, flat, isothermal plate as Formula (27).

$$\overline{Nu_\tau} = \frac{Nu'_0\, Re_F\, \overline{f_\tau}}{\sqrt{3}} \sqrt{\frac{Pr/\sqrt{162}+1}{\sqrt{162}\, Pr\, \overline{f_\tau}+1}} \sqrt[3]{\frac{Pr/\Xi}{\|1, 1/Pr\|_3}} \qquad \sqrt{162} \equiv 9\sqrt{2} \approx 12.7 \tag{27}$$

$$\overline{f_\tau} = \frac{2^{-5/4}}{\left[\mathrm{W}_0\left(Re_F/\sqrt{3}\right) - 1\right]^2} \qquad \Xi = \left\| 1,\ \frac{0.5}{Pr} \right\|_{\sqrt{1/3}} \qquad Nu'_0 = \frac{2^4}{\pi^2\, \sqrt[4]{2}} \approx 1.363 \tag{28}$$

- W_0 is the principal branch of the Lambert W function, defined as $\mathrm{W}_0(\varpi \exp \varpi) = \varpi$ when $\varpi \geq 0$.
- In Formula (28), $2^{-5/4}$ replaces the earlier $\sqrt[3]{2}/3$ coefficient from Jaffer [18], a +0.11% change.

5.3 **Smooth Plate.** Laminar and turbulent flow are not mutually exclusive, Jaffer [18] derives the average $\overline{Nu_\sigma}$ along a smooth, flat, isothermal plate as Formula (29), where critical Reynolds number Re_c is the upper bound of purely laminar flow.

$$\overline{Nu_\sigma} = \left\| \overline{Nu_\lambda}(Re_F),\ \overline{Nu_\tau}(Re_F) - \overline{Nu_\tau}\left(\|Re_F,\ \sqrt{\gamma}\, Re_c\, \|_{-8/\gamma} \right) \right\|_\gamma \tag{29}$$

$$\gamma = 1 + \exp_2\left(-Pr^{-\sqrt{1/2}}\right) \tag{30}$$

- Figure 9 shows a graph of $1 < \gamma < 2$.

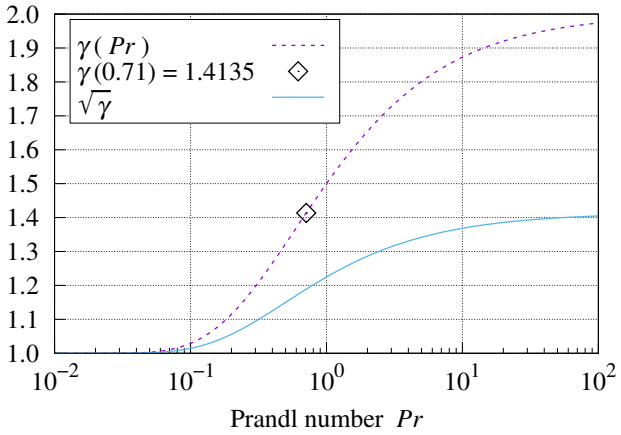

Figure 9 $\gamma(Pr)$ **and** $\sqrt{\gamma(Pr)}$

5.4 **Fluid Properties.**

- The fluid's thermal conductivity k and kinematic viscosity ν are computed for fluid at the average of the plate temperature and free-stream temperature (far from the plate).
- From Žukauskas and Šlančiauskas [19], the fluid's effective Prandtl number $Pr = Pr_w^{1/4}\, Pr_\infty^{3/4}$, where Pr_w is at plate temperature and Pr_∞ is at free-stream temperature.

6. Mixed Convection

Inclined mixed convection derives from upward, downward, and vertical convection components.

6.1 **Upward Facing Plate.** Figure 2 shows that flow is inward above the heated surface. Laminar forced flow parallel to the surface will combine with the leading edge inward flow as the ℓ^1-norm. But flow turns upward near the plate center. Their heat flows are perpendicular, suggesting the ℓ^2-norm. The geometric mean of 1 and 2 is $\sqrt{2}$, suggesting that $\overline{U^*}$ and $\overline{U_F}$ should be combined as the $\ell^{\sqrt{2}}$-norm, $\|\overline{U_F}, \overline{U^*}\|_{\sqrt{2}}$.

Turbulent forced flow should combine with $\overline{U^*}$ as the ℓ^2-norm, $\|\overline{U_F}, \overline{U^*}\|_2$.

Proposed[2] Formula (31) gradually transitions between $p^* = \sqrt{2}$ and $p^* = 2$ as a function of Re_F/Re_c:

$$p^*\left(\frac{Re_F}{Re_c}\right) = \exp_{\sqrt{2}}\left(1 + \exp_2\left(-\left[\frac{Re_c}{Re_F}\right]^2\right)\right) \tag{31}$$

6.2 **Downward Facing Plate.** Figure 3 shows that flow is outward immediately beneath the heated surface. Forced flow parallel to this surface is thus incompatible with downward natural convection $\overline{U_R}$. Moreover, downward natural convection involves reverse flows further from the plate. Thus downward natural convection is easily disrupted by a forced flow.

The natural and forced fluid flows will compete for surface area. Formula (11) shows that $\overline{Nu_R}$ is proportional to $\sqrt[5]{Ra_R}$, suggesting that $\overline{U_R}$ and $\overline{U_F}$ be combined using the ℓ^5-norm, $\|\overline{U_F}, \overline{U_R}\|_5$.

6.3 **Vertical Plate.** Formula (29) represents the "pierced-laminar" model where laminar flow is pierced by vortexes more frequently as forced flow increases. The vertical mode of mixed convection will introduce Re (as opposed to $\overline{Nu}$) mixing into the laminar component of pierced-laminar flow.

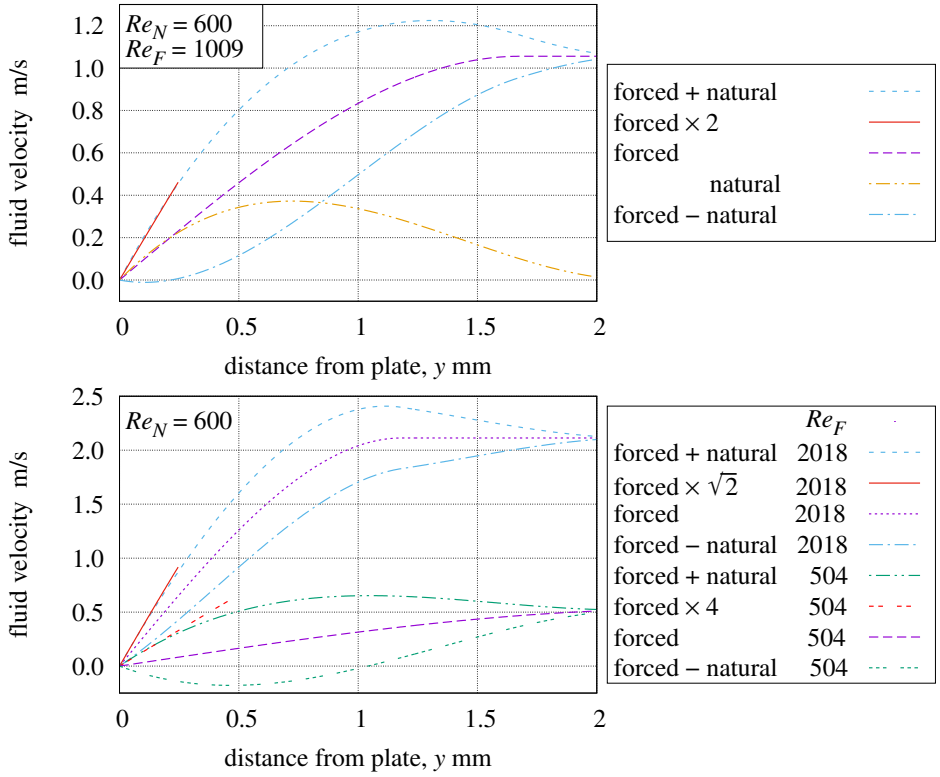

Figure 10 Laminar velocity profiles

6.4 **Laminar Velocity Profiles.** Formulas from Lienhard and Lienhard [20] lead to forced velocity profile Formula (32) and natural convection velocity profile Formula (33). Both are the velocity at horizontal distance $0 < y < \delta_\lambda$ from the vertical plate mid-line. Positive $u(y)$ is in the direction of forced flow; δ_λ is the

[2] $p^* > \sqrt{2}$ has not yet been tested.

boundary layer thickness at the height mid-line. The bulk forced flow velocity is $u_F = \nu\, Re_F/L$, where ν is the fluid's kinematic viscosity. Effective natural flow speed $u_N = \nu\, Re_N/L$ is the forced flow speed which would produce the same heat transfer as the natural convection.

$$\frac{u(y)}{u_F} \approx \frac{1}{4}\,\frac{y}{\delta_\lambda}\left\{3 - \left[\frac{y}{\delta_\lambda}\right]^2\right\} \qquad 0 < y < \delta_\lambda \approx \frac{4.92\,L}{\sqrt{Re_F}} \tag{32}$$

$$\frac{u(y)}{u_N} \approx 4\,\frac{y}{\delta_\lambda}\left[1 - \frac{y}{\delta_\lambda}\right]^2 \qquad 0 < y < \delta_\lambda \approx \frac{4.92\,L}{\sqrt{Re_N}} \tag{33}$$

The upper plot in Figure 10 shows the theoretical velocity profiles of laminar forced and natural convection adjacent to a vertical 12 mm disk plate at its height mid-line, as well as their sum and difference profiles. $Re_F = 2^{3/4}\,Re_N$ produced cancellation of "forced − natural" close to the plate. As a consequence, it is not surprising that "forced + natural" is nearly identical to "forced × 2" where $0 < y < 0.25$ mm.

The lower plot in Figure 10 also shows the theoretical velocity profiles of laminar forced flow, and that flow combined with natural flow. The forced Re_F values are double and half of 1009 from the upper plot.

While the velocity along one horizontal line on the plate can be zero, fluid along the rest of the plate moves. Even in the absence of net flow along the plate, the constant term of natural convection will transport heat. Thus, not all of the natural convection component can be reduced by opposing forced flow. Desired are formulas which satisfy these conditions:

- Opposed vertical flow heat transfer reaches its (non-zero) minimum near $Re_F/Re_N = 2^{3/4} \approx 1.682$.
- With $Re_F = 0$, heat transfer is identical to $\overline{Nu_N}$ Formula (24).
- As Re_F/Re_N increases, heat transfer approaches $\overline{Nu_\sigma}$ Formula (29).
- The formulas are continuously differentiable in all variables.

6.5 **Vertical Plate Mixed Convection.** Formula (29) is adapted to vertical plate mixed convection in Formula (34) by replacing $\overline{Nu_\lambda}(Re_F)$ with $\overline{Nu'}/2 + \overline{Nu_\lambda}(Re_\lambda)$, and replacing Re_F by Re_τ Formula (35). Forced γ is from Formula (30).

$$\overline{Nu_V} = \left\| \frac{\overline{Nu'}}{2} + \overline{Nu_\lambda}\,(Re_\lambda)\,,\ \overline{Nu_\tau}(Re_\tau) - \overline{Nu_\tau}\left(\,\|Re_\tau,\ \sqrt{\gamma}\,Re_c\,\|_{-8/\gamma}\right)\right\|_\gamma \tag{34}$$

$$Re_\tau = \sqrt{{Re_\lambda}^2 + \eta^2\,{Re_F}^2} \qquad \eta^2 = 1 - \sqrt{1/2} \approx 0.293 \tag{35}$$

$\overline{Nu'}/2 + \overline{Nu_\lambda}(Re_\lambda)$ totals half of the natural convective component with the heat transfer of the forced–natural mixture $\overline{Nu_\lambda}(Re_\lambda)$. Formula (36) Re_λ is the magnitude of the vector sum of $Re_{N/2}$ and $\zeta\,Re_F$, where $Re_{N/2}$ is the effective forced flow producing natural convective heat transfer $\overline{Nu'}/2$:

$$Re_\lambda = \sqrt{\left[Re_{N/2} + \cos(\psi)\,\zeta\,Re_F\right]^2 + \left[\,\sin(\psi)\,\zeta\,Re_F\,\right]^2} \tag{36}$$

$0° < \psi \le 180°$ is the angle of forced flow from the zenith. Although $\cos(\psi)$ is negative with opposing flow $90° < \psi \le 180°$, the radicand of Formula (36) is always positive.

Combining Re_F with $Re_{N/2}$ instead of Re_N under-weights Re_F when $Re_F \ll Re_{N/2}$ and over-weights Re_F when $Re_F \gg Re_{N/2}$ in vertical flows. Horizontal forced flow ($\psi = 90°$) always over-weights $Re_F > 0$. The weightings are corrected in Formula (36) by the Re_F coefficient ζ:

$$\zeta = \exp_2\left(\frac{3}{4}\,\cos^2\psi\,\exp_2\left(-\frac{1}{2}\,\left[\frac{Re_F}{Re_{N/2}}\right]^{4/3}\right) - \frac{1}{4}\right) \tag{37}$$

Figure 11 plots vertical flow Re_F coefficient ζ as a function of $Re_F/Re_{N/2}$ and ψ. It ranges from $\zeta(0, 0°) = \sqrt{2} \approx 1.414$ to $\zeta(\infty, \psi) = 1/\sqrt[4]{2} \approx 0.841$. Note that $\eta^2 + \zeta^2(\infty, \psi) = 1$, assuring that Re_τ approaches Re_F when $Re_F/Re_{N/2} \gg 1$.

6.6 **Composing Functions with the ℓ^p-norm.** The ℓ^p-norm is typically used with heat transfer inputs. In taking the square root of the sum of squares Formula (36) is equivalent to an ℓ^2-norm whose inputs are Reynolds numbers. What can be inferred about the heat transfer behavior of $\overline{Nu_\lambda}(Re)$?

According to Formula (2), $\|F, F\|_p \equiv 2^{1/p}\, F$. Thus the effective p of (laminar) $\overline{Nu_\lambda}(Re)$ is:

$$1/\log_2\left(\frac{\overline{Nu_\lambda}(\|Re, Re\|_{p_{Re}})}{\overline{Nu_\lambda}(Re)}\right) \tag{38}$$

Formula (38) is plotted in Figure 12. At low Re values, where $\overline{Nu_\lambda}$ is nearly linear, $\overline{Nu_\lambda}(Re)$ has an effective $p \approx 2$. At large Re values, $\overline{Nu_\lambda}(Re)$ is roughly proportional to $\sqrt{Re}$ and effective $p \approx 4$, behaving like:

$$\left\| \overline{Nu_\lambda}\left(\left|Re_{N/2} + \cos(\psi)\,\zeta\, Re_F\right|\right) \;,\; \overline{Nu_\lambda}\left(\left|\sin(\psi)\,\zeta\, Re_F\right|\right) \right\|_4 \tag{39}$$

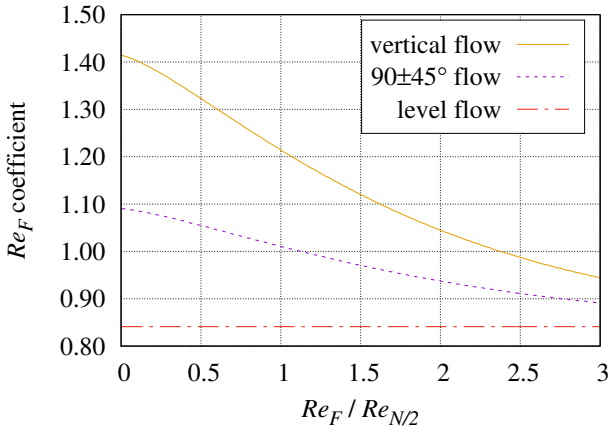

Figure 11 Vertical plate laminar Re coefficients

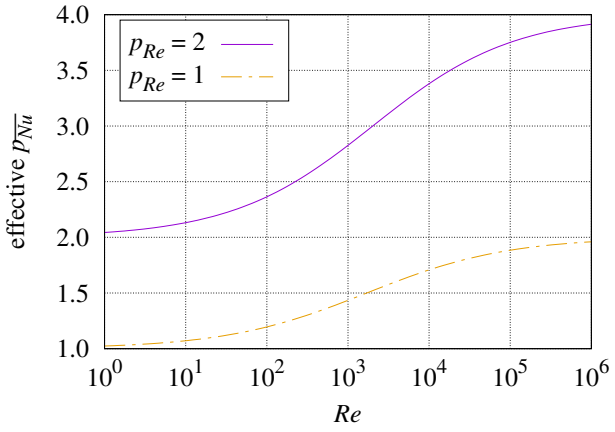

Figure 12 Effective p of $\overline{Nu_\lambda}$

6.7 **Corner Cases.** Table 5 lists the asymptotic p for plate and flow orientations which are horizontal or vertical. The rough plate entries are from Jaffer and Jaffer [16].

- θ is the angle of the plate from vertical;
- ψ is the angle between the forced flow and the zenith;
- p_{Re} is the p combining Reynolds numbers along a smooth vertical plate;
- $p(0)$ is for laminar forced flow along a smooth plate;
- $p(\infty)$ is for turbulent forced flow along a smooth plate;
- $p(\ll)$ is $p(Re_F/Re_N)$ for forced flow along a rough plate when $Re_F/Re_N \ll 1$;
- $p(\gg)$ is $p(Re_F/Re_N)$ for forced flow along a rough plate when $Re_F/Re_N \gg 1$.
- (?) marks the cases which have not yet been tested.

Table 5 Corner cases p

Description	**Face**	**Flow**	**Laminar**	**Smooth**		**Rough**	
	θ	ψ	p_{Re}	$p(0)$	$p(\infty)$	$p(\ll)$	$p(\gg)$
upward facing plate	−90°	90°		$\sqrt{2}$	2(?)	2	2
aiding vertical plate	+0°	0°	1			$\sqrt{3}$	3
vertical plate, level flow	+0°	90°	2			2	2
opposing vertical plate	+0°	180°	1			3	$\sqrt{3}$
downward facing plate	+90°	90°		5	5(?)	5	5

7. Laminar Mixed Convection From a Disk

Although more complicated to model than rectangular plates, the small size of thermistor disks enables them to operate at Re values low enough to thoroughly explore laminar mixed convection.

The forced convection thermal conductance from a disk face and its rim are $\overline{U_\bullet}$ and $\overline{U_\circ}$ respectively:

$$\overline{U_\bullet} = \frac{k\,A_\bullet}{L'}\,\overline{Nu_\sigma} \qquad \overline{U_\circ} = \pi\,k\,t\,\overline{Nu_\circ} \tag{40}$$

where $\overline{Nu_\circ}$ is the Churchill-Bernstein cylinder formula from Lienhard and Lienhard [20] (p. 428):

$$0.3 + \frac{0.62\,\sqrt{Re_d}\,\sqrt[3]{Pr}}{\sqrt[4]{1+[0.4/Pr]^{2/3}}}\left[1+\left[\frac{Re_d}{282\times10^3}\right]^{5/8}\right]^{4/5} \qquad Re_d\,Pr > 0.2 \tag{41}$$

The 0.3 constant term in Formula (41) is clearly natural convection, not forced convection. This investigation uses $\overline{Nu_\circ}$ Formula (42):

$$\overline{Nu_\circ} = \frac{0.62\,\sqrt{Re_d}\,\sqrt[3]{Pr}}{\sqrt[4]{1+[0.4/Pr]^{2/3}}}\left[1+\left[\frac{Re_d}{282\times10^3}\right]^{5/8}\right]^{4/5} \tag{42}$$

Figure 13 shows Formula (41) and Formula (42) at three values of Pr.

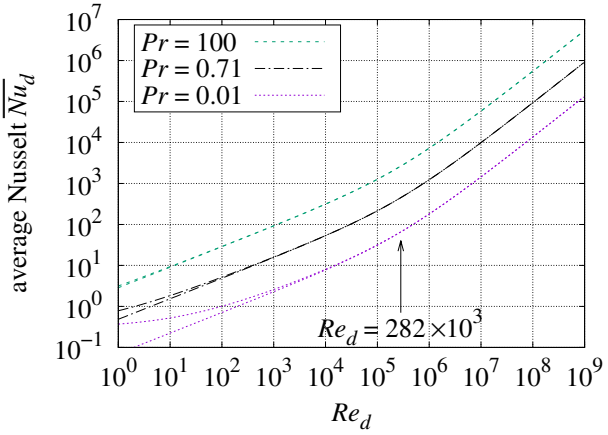

Figure 13 Forced across cylinder

7.1 **Vertical Disk.** Formula (43) defines the mixed convection conductance of the vertical rim $\overline{U_\parallel}$ by pairing the vertical component of forced rim flow, $|\cos\psi|\,\overline{U_\circ}$, with natural convection from the rim's sides, $2\,\overline{U_|}$, and pairing the horizontal component of forced rim flow, $|\sin\psi|\,\overline{U_\circ}$, with natural convection from the rim's top and bottom quarters, $\overline{U_\cup} + \overline{U'}\,t/d$.

$$\overline{U_\parallel} = \left\| |\cos\psi|\,\overline{U_\circ}\ ,\ 2\,\overline{U_|} \right\|_1 + \left\| |\sin\psi|\,\overline{U_\circ}\ ,\ \overline{U_\cup} + \frac{t}{d}\,\overline{U'} \right\|_2 \tag{43}$$

$\overline{Nu_V}$ Formula (34) models the mixing of forced flow $\overline{U_\bullet}$ and natural convection $\overline{U'}$. The mixed convective conductance of a vertical disk is thus:

$$2\,\frac{k\,A_\bullet}{L'}\,\overline{Nu_V}(\psi) + \overline{U_\parallel} \tag{44}$$

with reuptake $\Phi\left[\cos^4\theta\,\overline{U_\cap} + \cos^8\theta\,\overline{U_\cup}\right]$ from Formula (19). Vertical disk reuptake coefficient $\Phi(t/d)$ is defined by Formula (18).

7.2 **Horizontal Disk.** Extrapolating Formula (23) to include laminar forced horizontal flow, sum the contributions from the upper face $\overline{U_\uparrow}$ and the lower face $\overline{U_\downarrow}$. Reuptake is $\sin^2\theta\,\overline{U_R}$ from Formula (24).

$$\overline{U_\uparrow} = \left\| \overline{U^*}\,,\,\overline{U_\bullet} \right\|_{\sqrt{2}} + S_\circ \left\| 4\,\frac{t}{d}\,\overline{U^*}\ ,\ \overline{U_\circ} \right\|_{\sqrt{2}} \tag{45}$$

$$\overline{U_{\downarrow}} = \left\| \overline{U_R} \, , \, \overline{U_{\bullet}} \right\|_5 + [1 - S_{\circ}] \left\| \overline{U_{=}} \, , \, \overline{U_{\circ}} \right\|_{\sqrt{2}} \tag{46}$$

7.3 **Inclined Disk.** The vertical rim conductance $\overline{U_{\parallel}}$ is split with swapped weights, $1 - S_{\circ}$ and $S_{\circ}$ versus $\overline{U_{\uparrow}}$ and $\overline{U_{\downarrow}}$ in order to balance $\overline{U_{\circ}}$. Proposed is Formula (47) for the mixed convective heat transfer from laminar forced flow parallel to a disk at inclination θ with angle of forced flow from the zenith ψ:

$$\begin{aligned} &\left\| \frac{k\,A_{\bullet}}{L'} \, \overline{Nu_V}(\psi) + [1 - S_{\circ}] \, \overline{U_{\parallel}} \, , \, \overline{U_{\uparrow}} \right\|_{16} \\ &+ \left\| \frac{k\,A_{\bullet}}{L'} \, \overline{Nu_V}(\psi) + S_{\circ} \, \overline{U_{\parallel}} \, , \, \overline{U_{\downarrow}} \right\|_{16} \\ &- \left\| \Phi \left[\cos^4\theta \, \overline{U_{\cap}} + \cos^8\theta \, \overline{U_{\cup}} \right], \, 2 \, |\sin\theta \, \cos\theta| \, \overline{U_{|}} \right\|_{16} \\ &- \left\| \sin^2\theta \, \overline{U_R} \, , \, 2 \, |\sin\theta \, \cos\theta| \, \overline{U_{|}} \right\|_{16} \end{aligned} \tag{47}$$

As with natural convection Formula (24), vertical disks at small Ra can have $\overline{U^*} > \overline{U'}$ or $\overline{U_R} > \overline{U'}$, causing Formula (47) to predict larger heat transfers than it should. To prevent this:

- $\overline{U_{\uparrow}}$ should be forced to 0 when $|\sin^3\theta| \, Ra^* < 1/4$;
- $\overline{U_{\downarrow}}$ should be forced to 0 when $|\sin^3\theta| \, Ra_R < 1/2$.

7.4 **Comparison With Measurements.** Kobus and Wedekind [7] measured mixed convection heat transfer from vertical thermistor disks in air. These measurements are presented in Figure 14. The measurements are points; lines are the present theory. The remaining figures in this section are of measurements by the present disk apparatus.

The first row of Figure 14 and all rows of Figure 15b have RMSRE less than 3% versus the present theory for a vertical disk in horizontal forced flow.

The second row of Figure 14 and all rows of Figure 16b have RMSRE less than 3.2% versus the present theory for a vertical disk in upward forced flow.

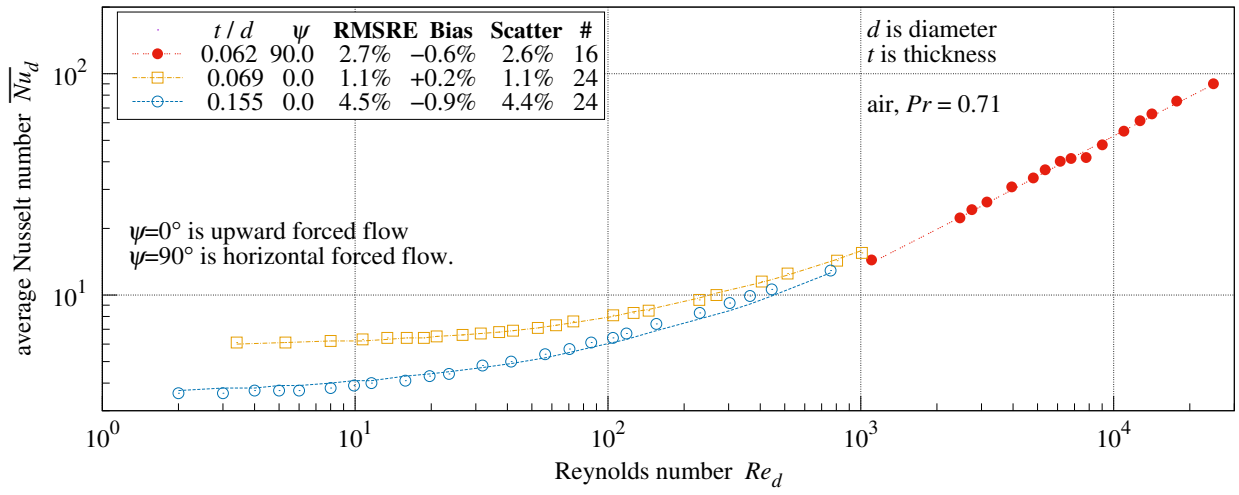

Figure 14 Kobus and Wedekind mixed convection heat transfer from vertical disk

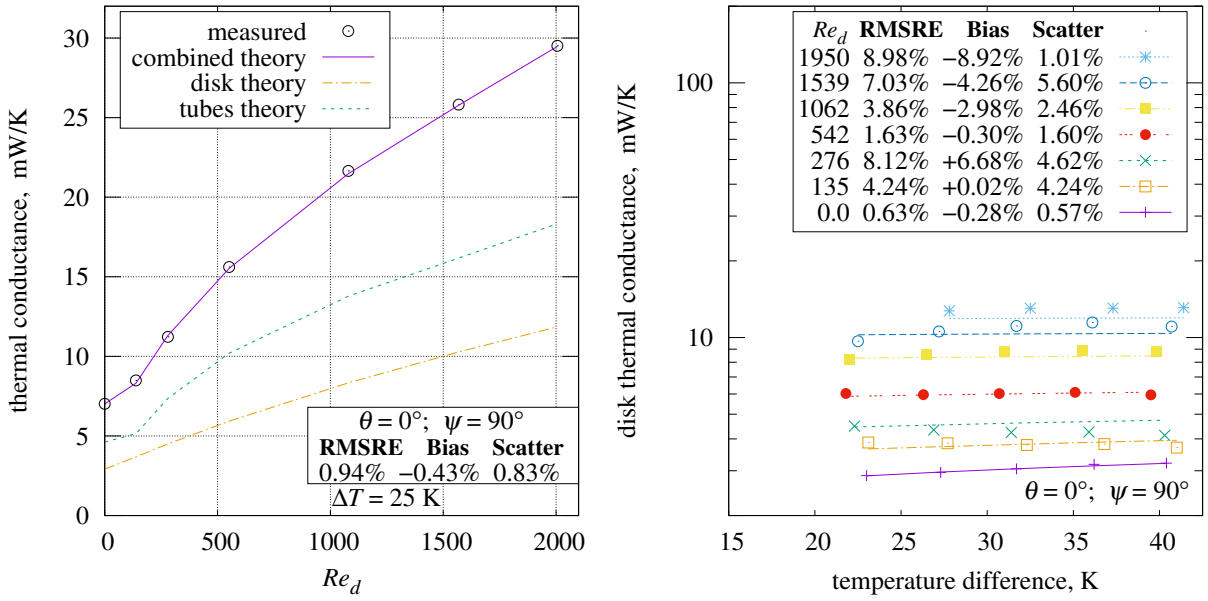

a **b**

Figure 15 Vertical disk in level forced flow (a) at $\Delta T = 25$ K (b) versus temperature

7.5 **Vertical disk in Level Forced Flow.** Figure 15a presents measurements of a vertical disk in horizontal forced flows between 0 m/s and 2.13 m/s at $\Delta T = 25$ K. These 25 K values are interpolated from measurements made with ΔT values slightly above and below 25 K. The "parasitics theory" traces predict heat transfer of the disk-holding fixture and its reuptake by the disk. Figure 15b shows the thermal conductances of the disk (measured total minus the predicted parasitics) across a range of ΔT values.

The auxiliary data[3] includes graphs of measured thermal conductance (combined disk and fixture).

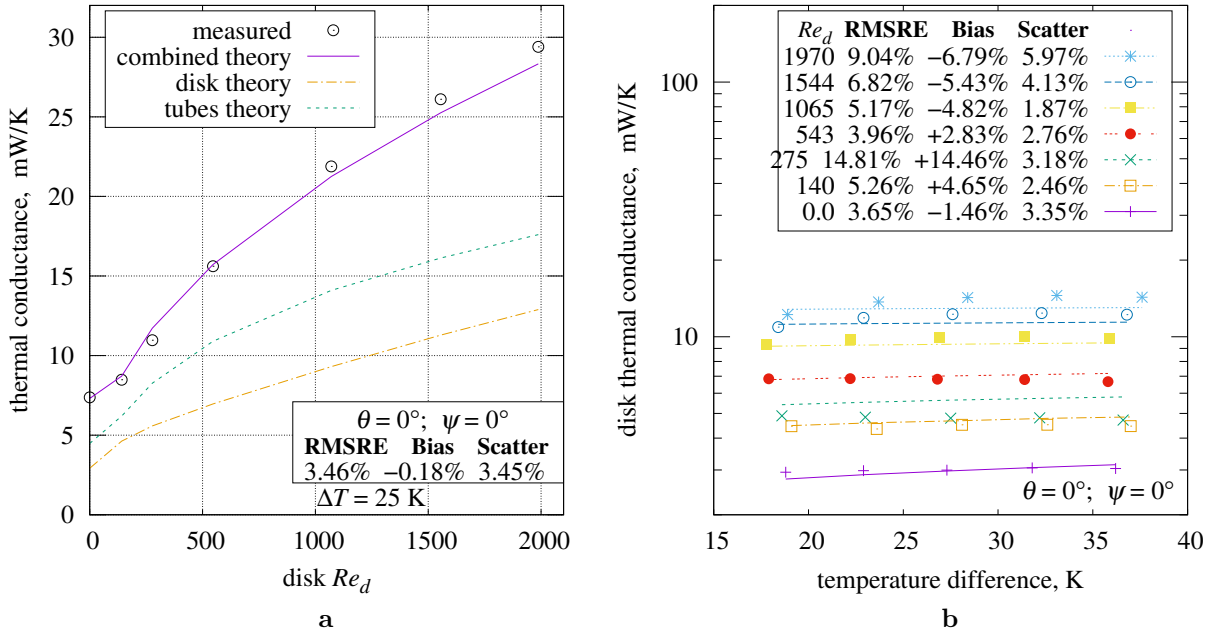

a **b**

Figure 16 Vertical disk in upward forced flow (a) at $\Delta T = 25$ K (b) versus temperature

7.6 **Vertical Disk in Upward Forced Flow.** Figure 16a shows mixed thermal conductance versus aiding forced Re_d at $\Delta T = 25$ K. Figure 16b shows disk thermal conductances across a range of ΔT values.

[3] `https://people.csail.mit.edu/jaffer/convect`

Note that the "parasitics theory" trace, which is fixture conductance minus the disk–fixture reuptake and wire heating discussed in (appendix) Section 13, is negative at $Re_d = 140$.

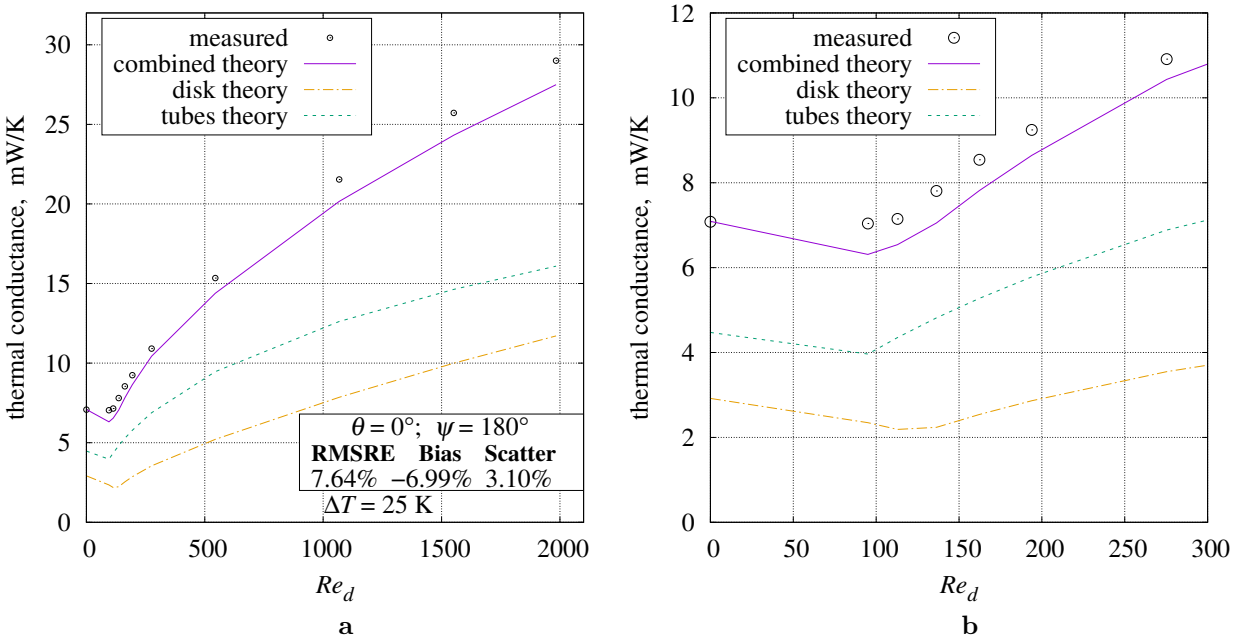

Figure 17 Vertical disk in downward forced flow (a) at $\Delta T = 25$ K (b) detail

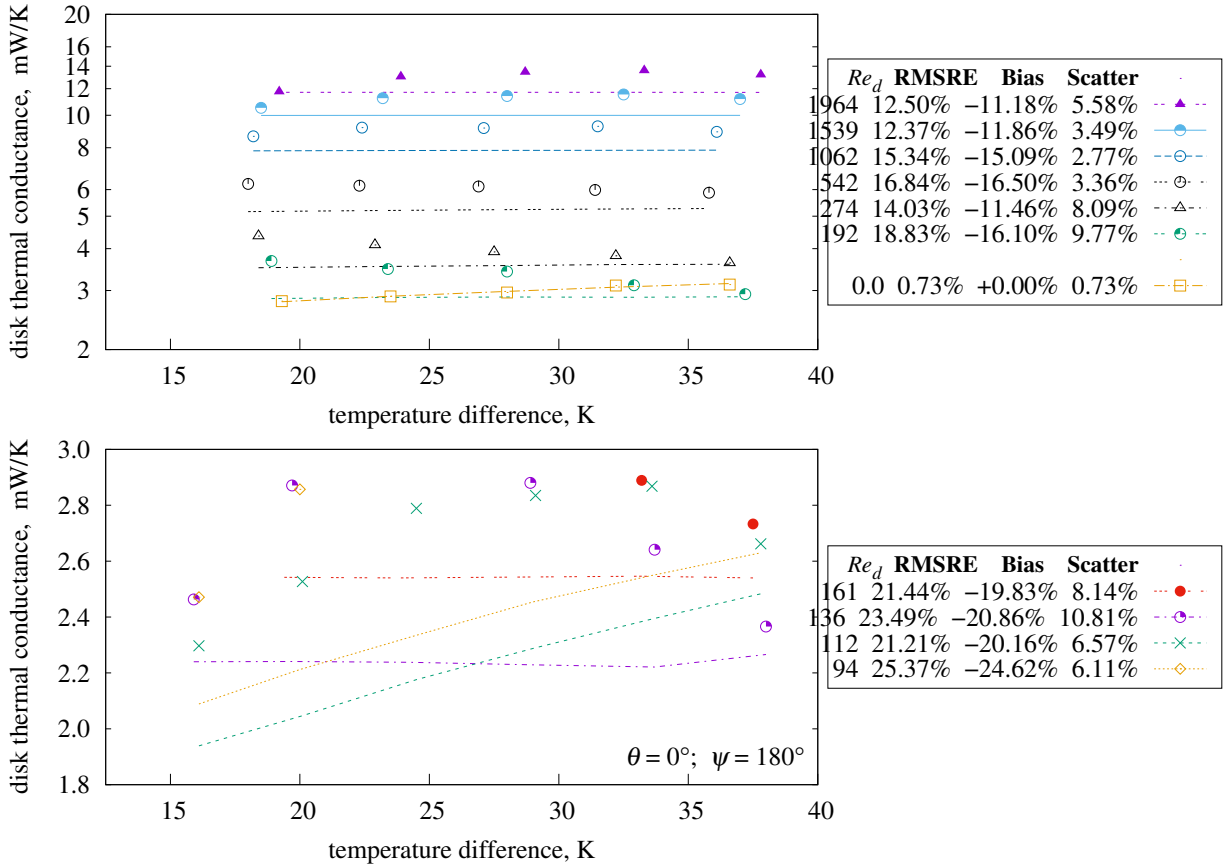

Figure 18 Vertical disk in opposing forced flow

7.7 **Vertical Disk in Downward Forced Flow.** Figure 17 shows mixed thermal conductance versus

the forced Re at $\Delta T = 25$ K. Figure 18 shows disk thermal conductances across a range of ΔT values.

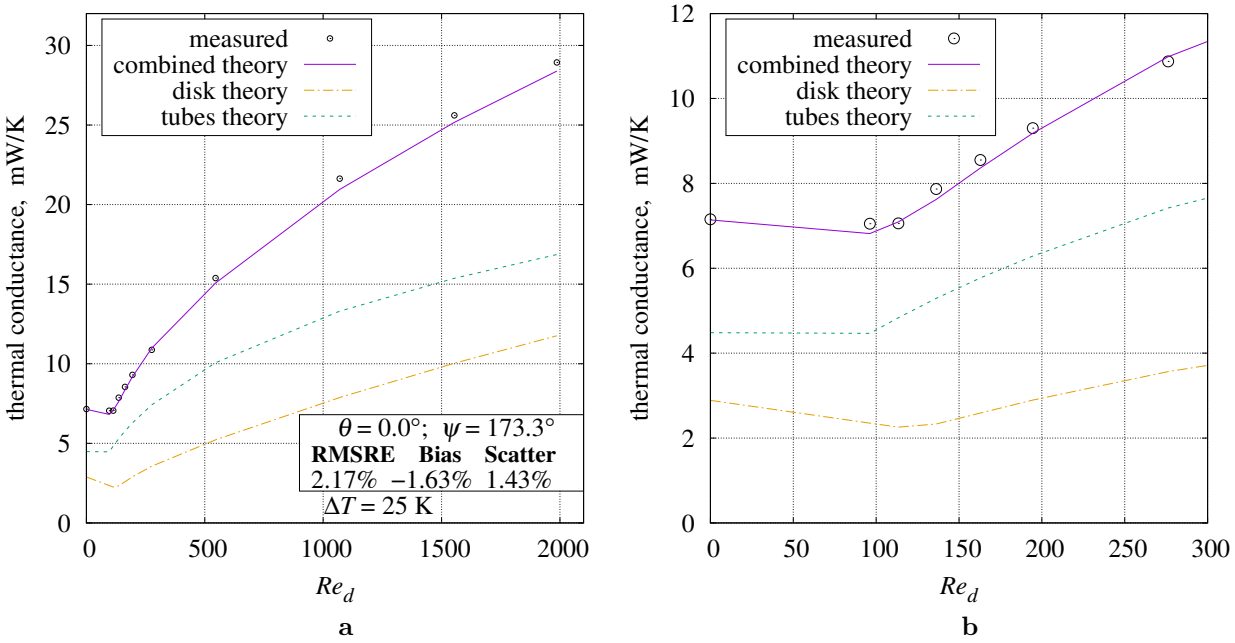

Figure 19 Vertical disk in nearly downward forced flow (a) at $\Delta T = 25$ K (b) detail

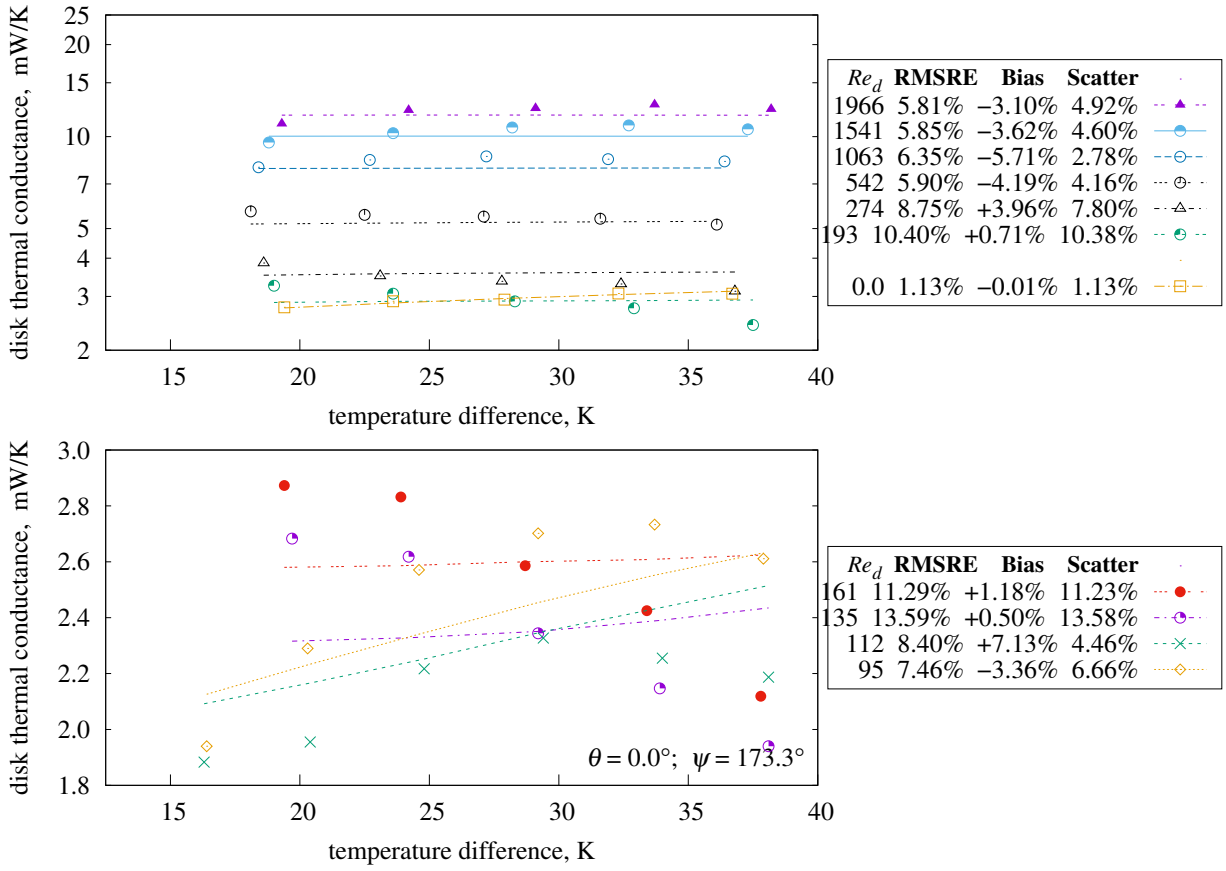

Figure 20 Vertical disk in nearly opposing forced flow

7.8 **Vertical Disk in Nearly Downward Forced Flow.** Figure 19 shows mixed thermal conductance versus forced Re at $\Delta T = 25$ K. Figure 20 shows disk thermal conductances across a range of ΔT values.

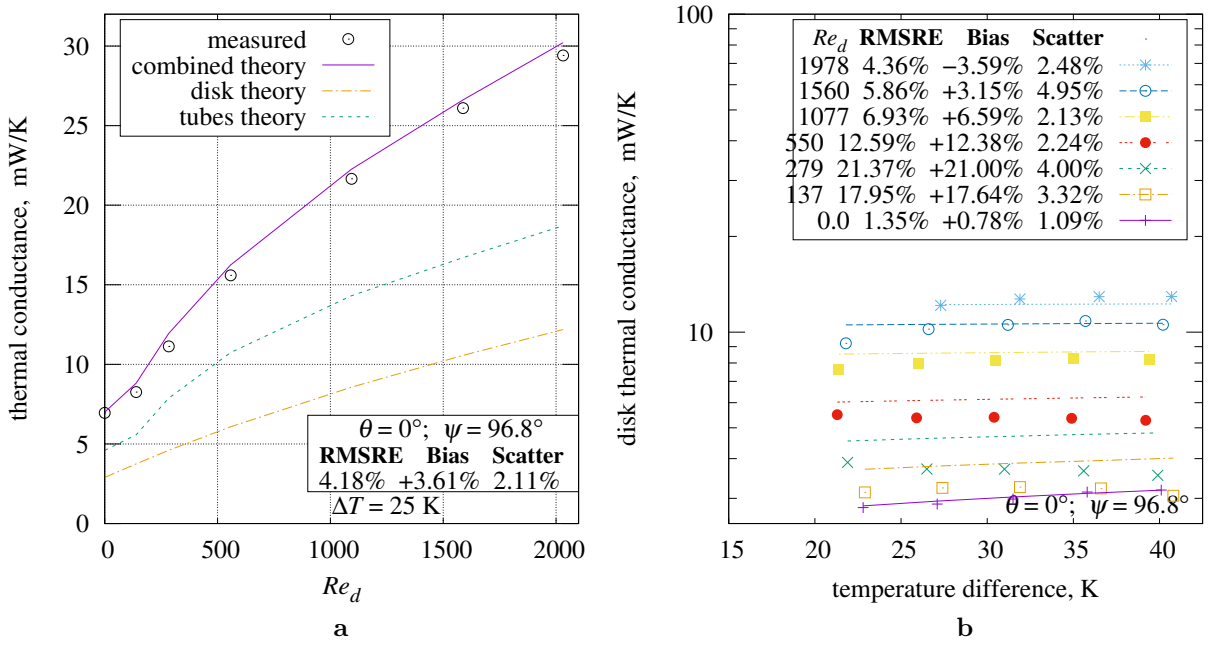

a **b**

Figure 21 Vertical disk in slightly downward forced flow (a) at $\Delta T = 25$ K (b) versus temperature

7.9 **Vertical disk in Slightly Downward Forced Flow.** Figure 21a presents measurements of a vertical disk in a flow pitched 6.8° downward between 0 m/s and 2.13 m/s at $\Delta T = 25$ K. Figure 21b shows the thermal conductances of the disk across a range of ΔT values.

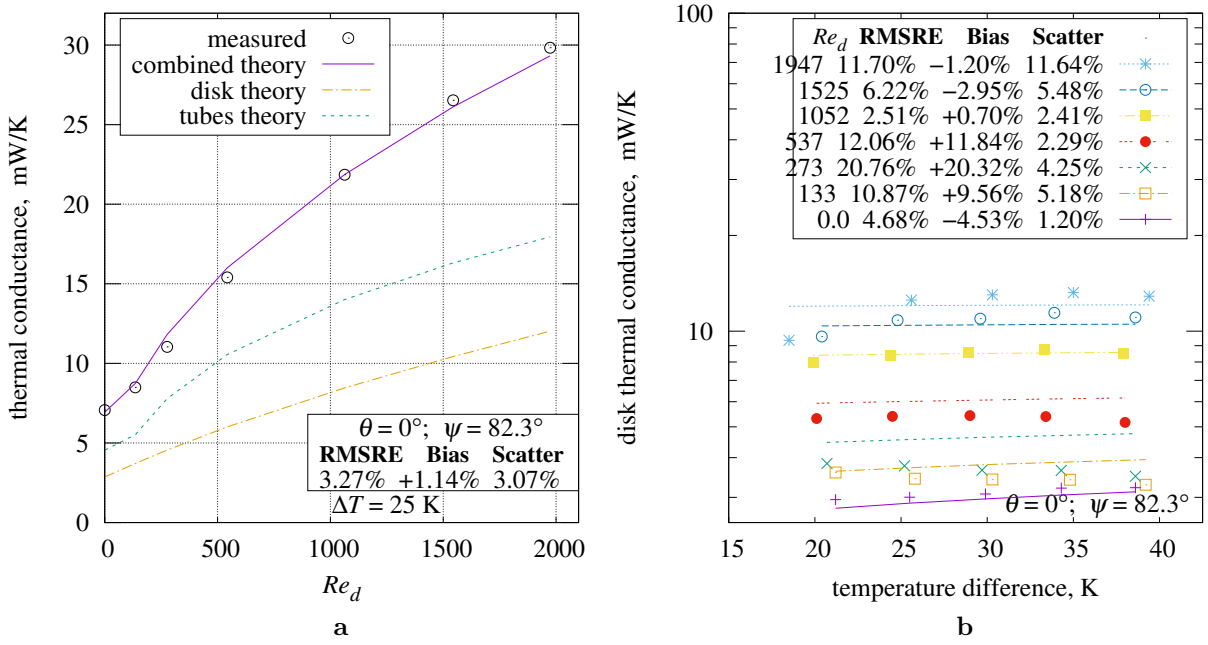

a **b**

Figure 22 Vertical disk in slightly upward forced flow (a) at $\Delta T = 25$ K (b) versus temperature

7.10 **Vertical Disk in Slightly Upward Forced Flow.** When the wind-tunnel with a vertical disk is pitched 82.6° from vertical, it produces Figures 22a, and 22b.

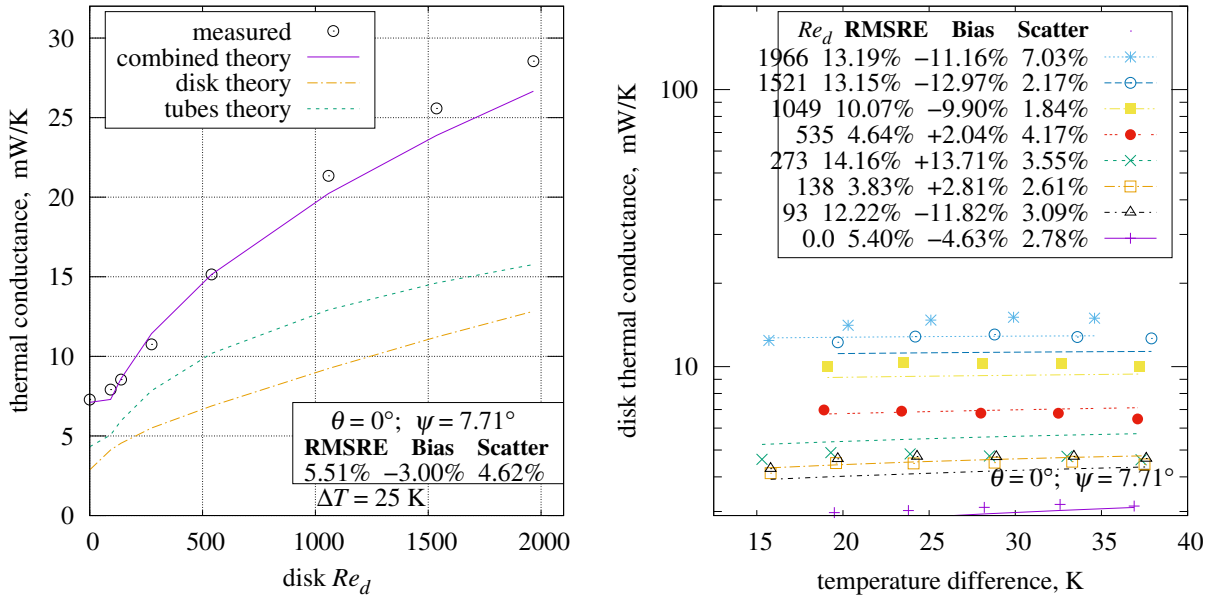

a **b**

Figure 23 Vertical disk in nearly upward forced flow (a) at $\Delta T = 25$ K (b) versus temperature

7.11 **Vertical Disk in Nearly Upward Forced Flow.** When the wind-tunnel with a vertical disk is pitched 7.7° from vertical, it produces Figures 23a, and 23b.

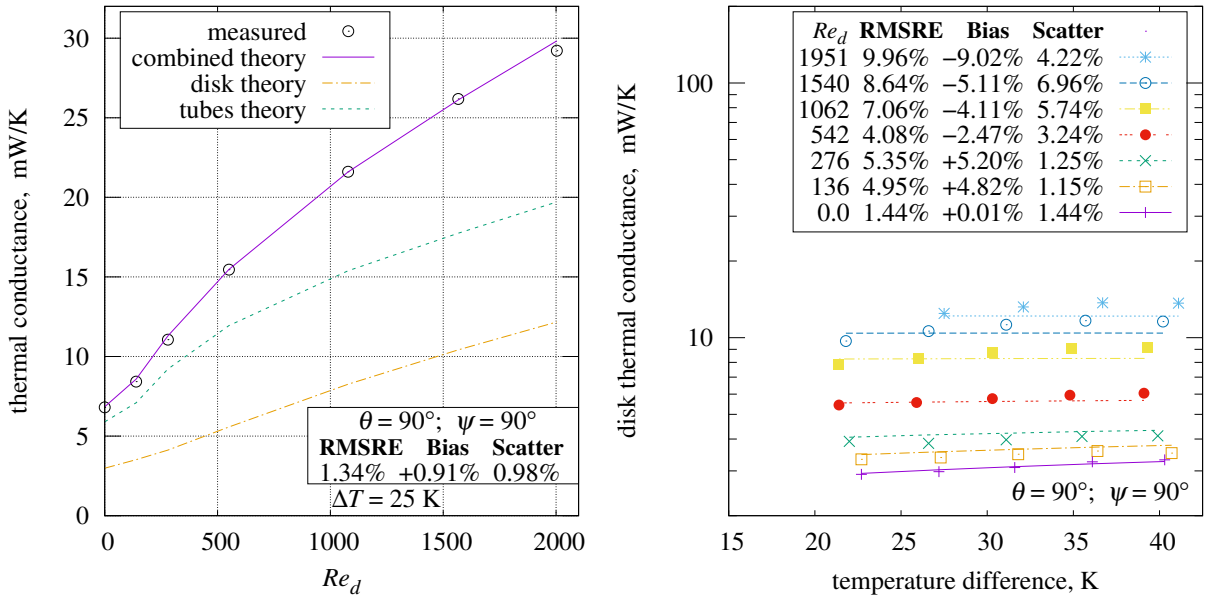

a **b**

Figure 24 Horizontal disk in level forced flow (a) at $\Delta T = 25$ K (b) versus temperature

7.12 **Horizontal Disk in Level Flow.** Figure 24a shows mixed thermal conductance versus the forced Re at $\Delta T = 25$ K. Figure 24b shows the disk thermal conductances across a range of ΔT values.

7.13 **Inclined Disk in Inclined Flow.** Pitching a horizontal disk strongly downward $\psi = 173.3°$ yields Figures 25a, 25b, and 26.

Pitching a horizontal disk slightly downward $\psi = 98.5°$ yields Figures 27a and 27b.

Pitching a horizontal disk slightly upward $\psi = 82.3°$ yields Figures 28a and 28b.

Pitching a horizontal disk strongly upward $\psi = 7.7°$ yields Figures 29a and 29b.

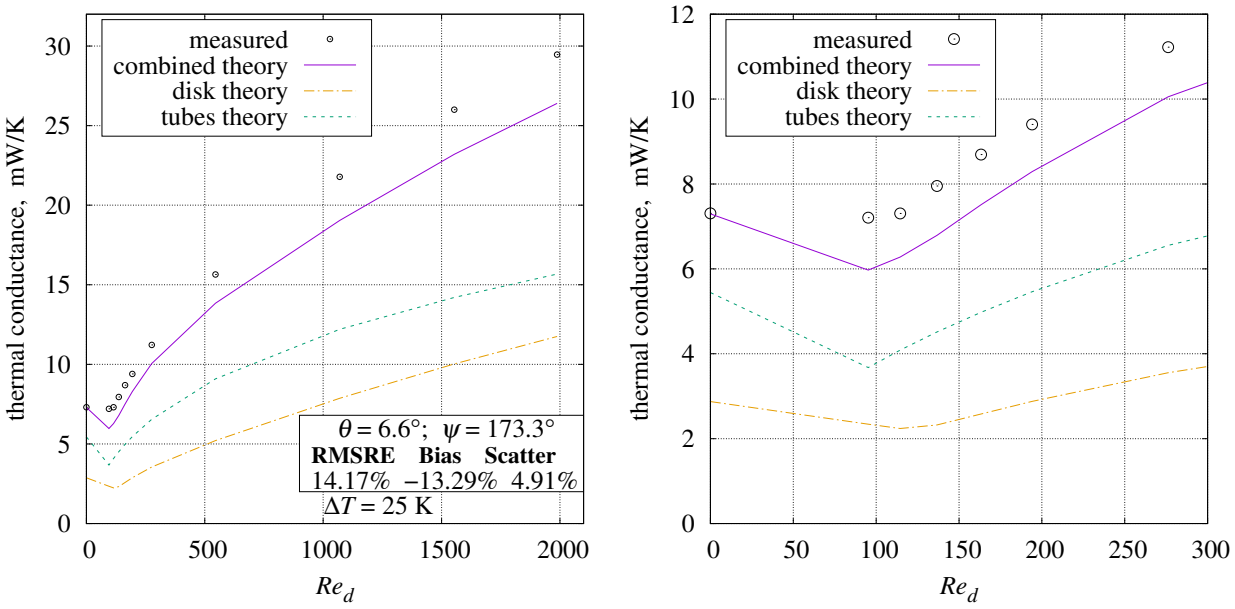

Figure 25 Nearly vertical disk in nearly downward forced flow (a) at $\Delta T = 25$ K (b) detail

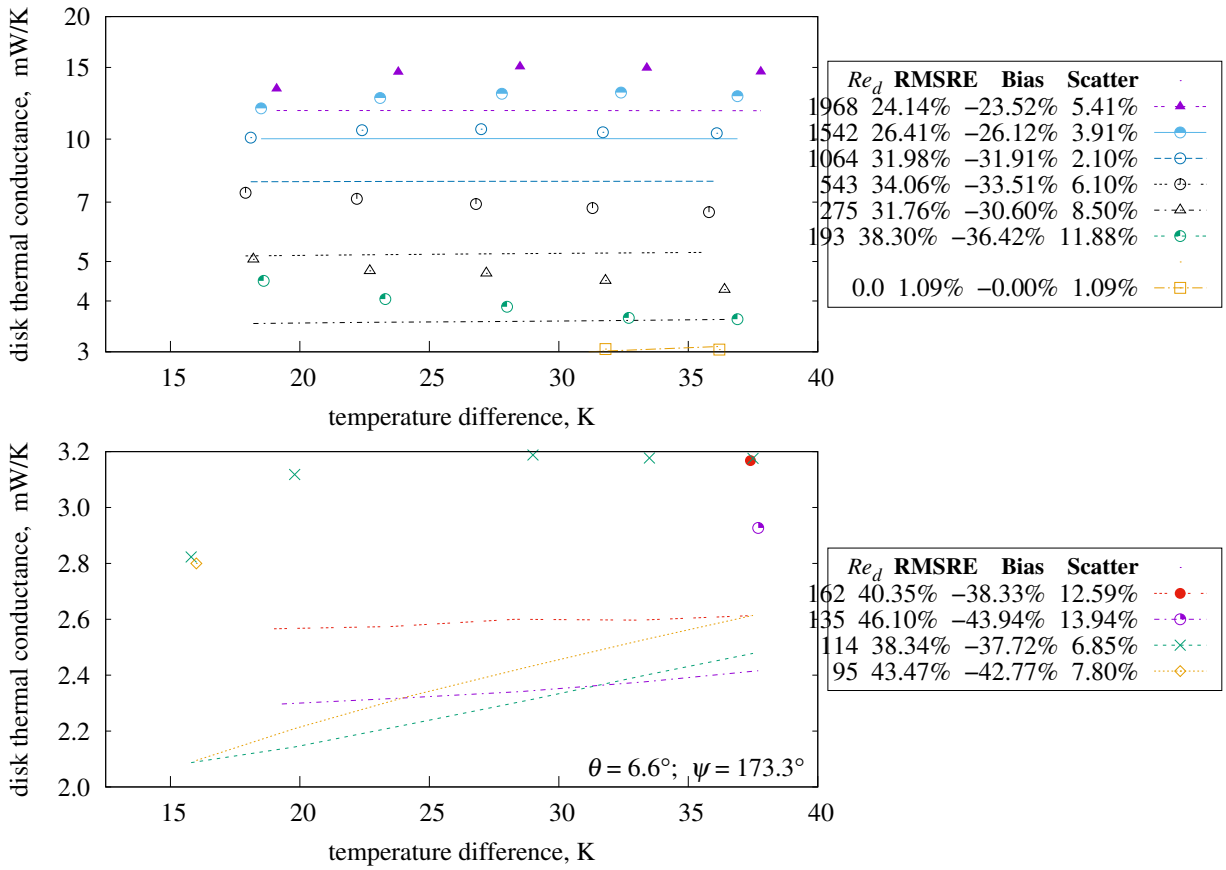

Figure 26 Nearly vertical disk in nearly opposing forced flow

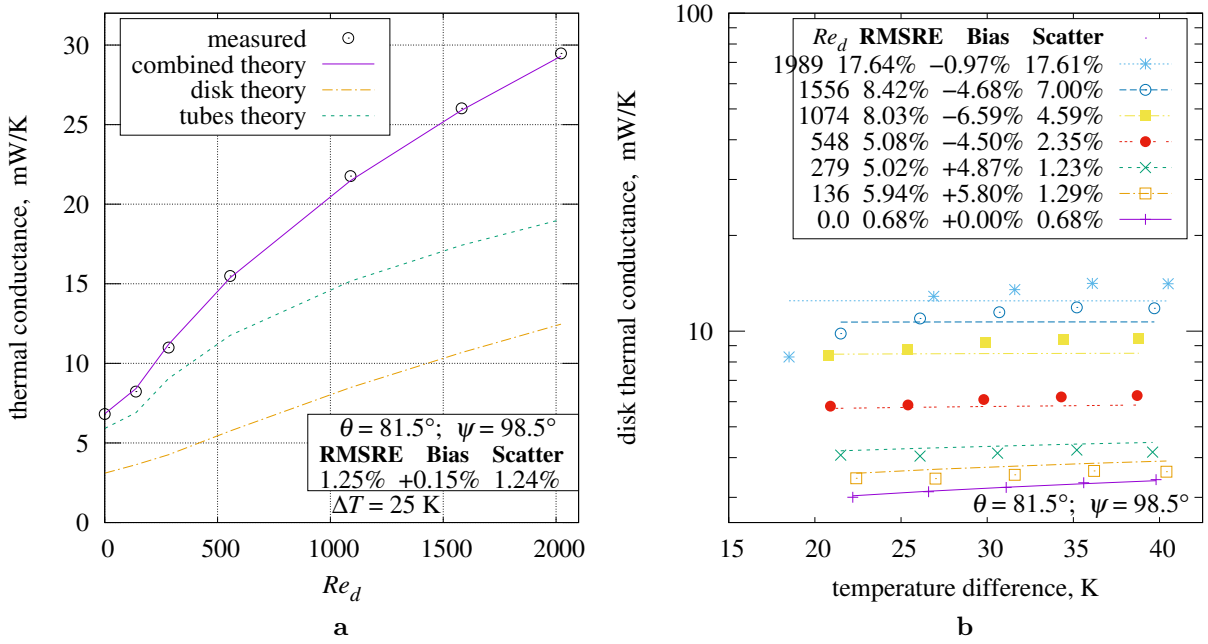

a **b**

Figure 27 Slightly downward pitched disk and forced flow (a) at $\Delta T = 25$ K (b) versus temperature

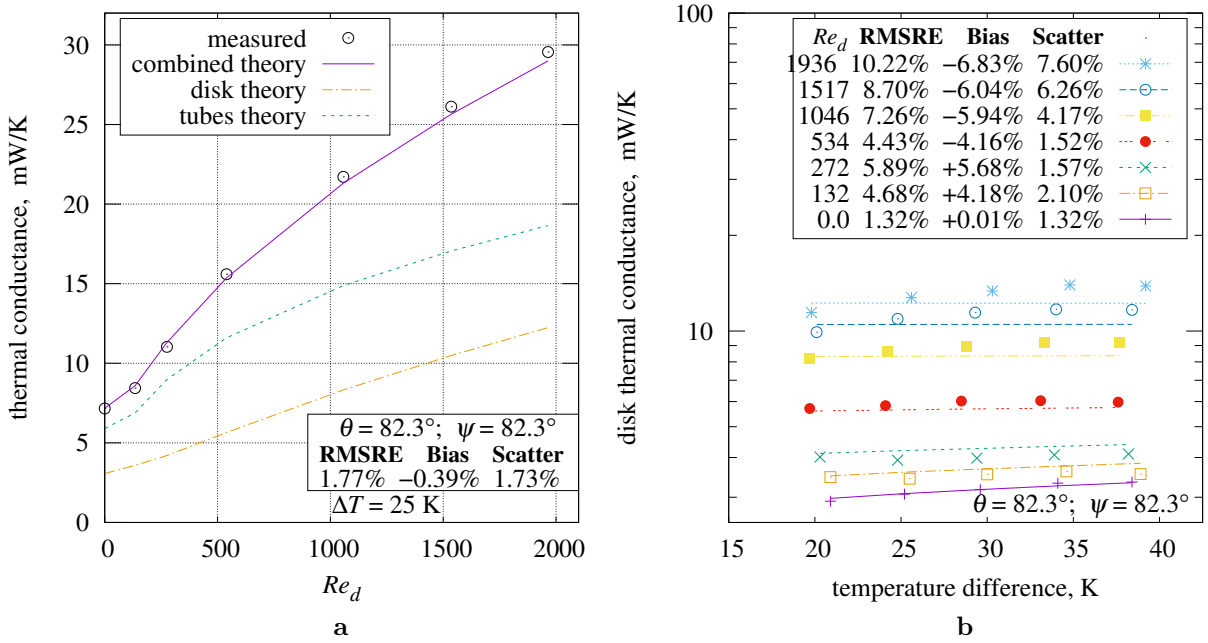

a **b**

Figure 28 Slightly upward pitched disk and forced flow (a) at $\Delta T = 25$ K (b) versus temperature

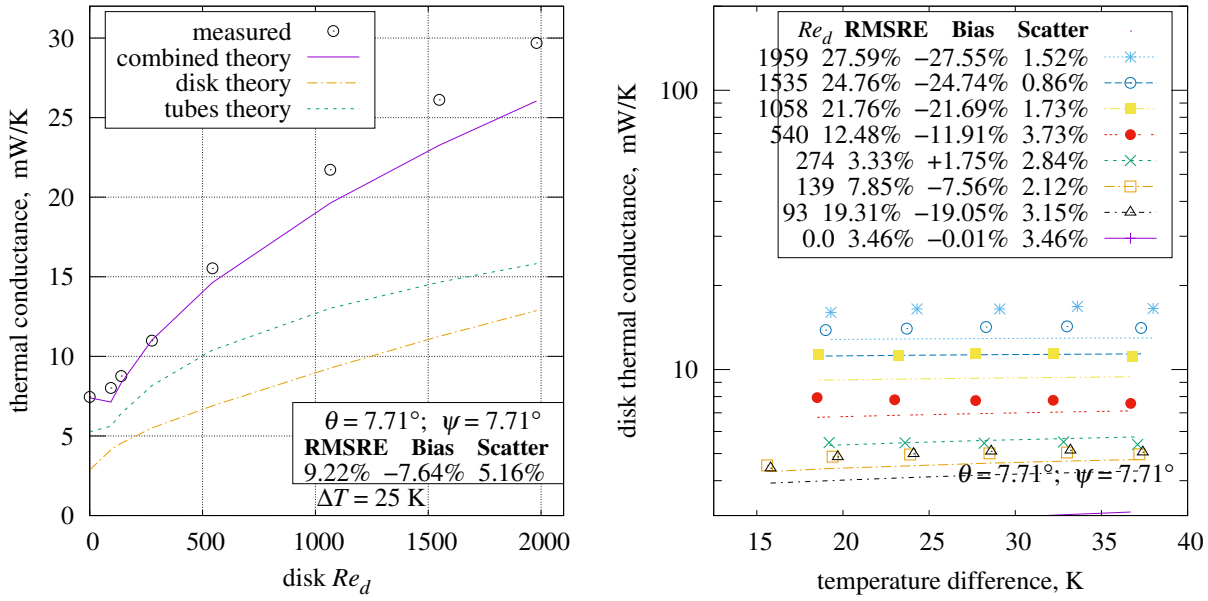

a **b**

Figure 29 Strongly upward pitched disk and forced flow (a) at $\Delta T = 25$ K (b) versus temperature

7.14 **Inclined Disk in Level Forced Flow.** When the wind-tunnel with a vertical disk is rolled 7° around the axis of flow, Figures 30a and 30b result.

Rolling the wind-tunnel 82.6° around the axis of flow produces Figures 31a, and 31b.

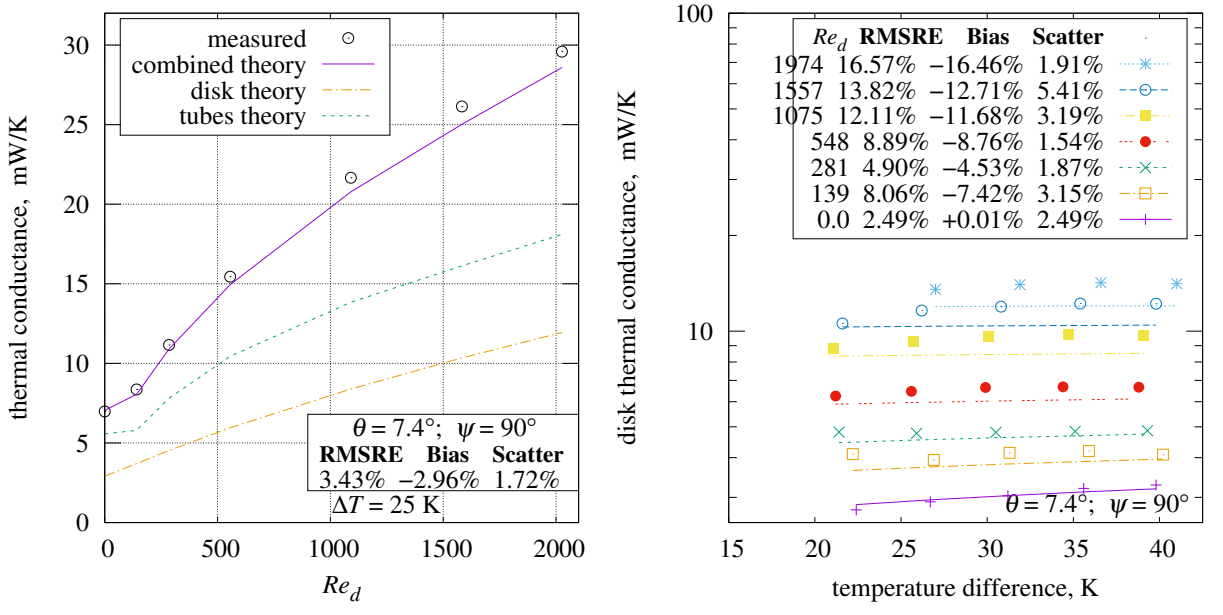

a **b**

Figure 30 Nearly vertical disk in level forced flow (a) at $\Delta T = 25$ K (b) versus temperature

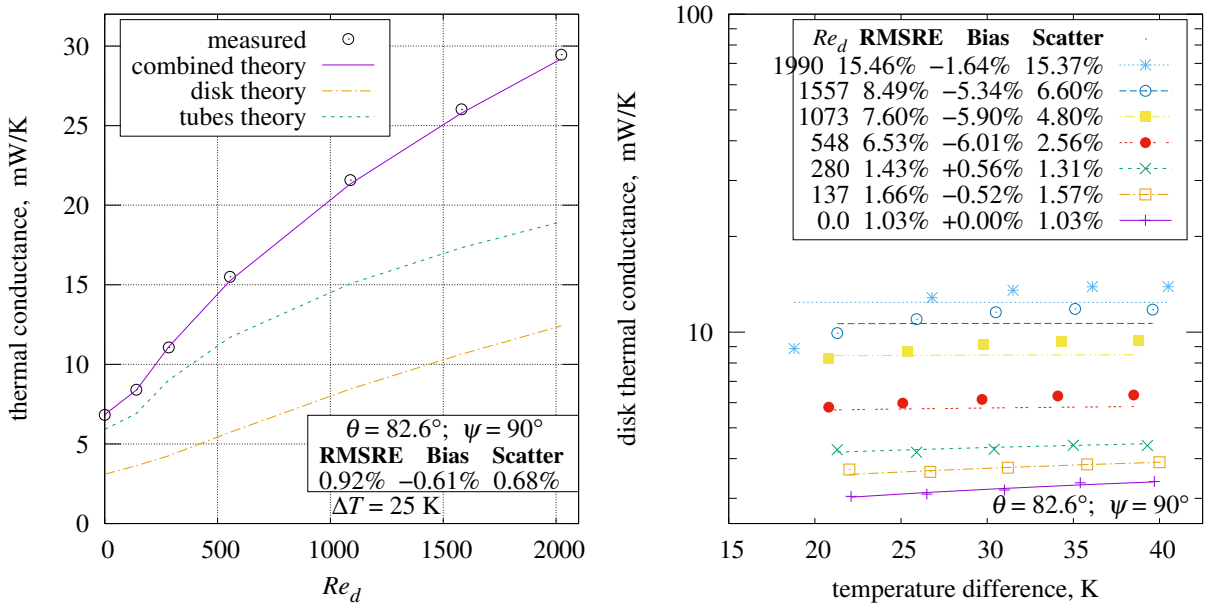

Figure 31 Mildly inclined disk in level forced flow (a) at $\Delta T = 25$ K (b) versus temperature

8. Transitional and Turbulent Mixed Convection

Attention now turns to larger plates which can generate turbulence from forced flow along them.

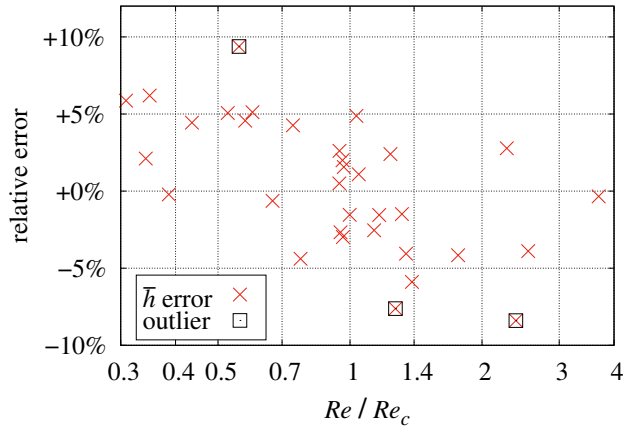

Figure 32 Relative error versus Re_F/Re_N

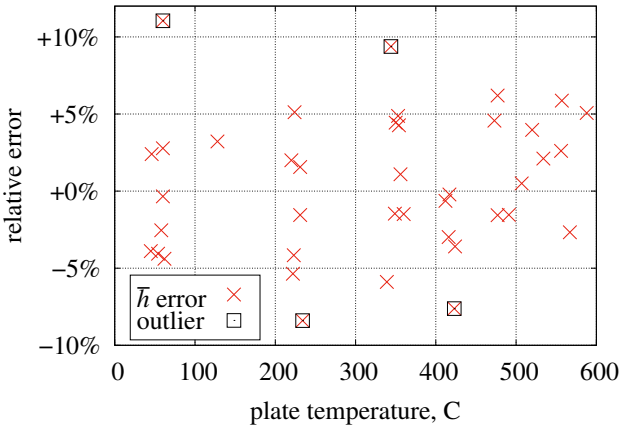

Figure 33 Relative error versus T

Table 6 Siebers et al. convection measurements

Source	Dimensions	θ	ψ	p	Re_c	RMSRE	Bias	Scatter	Used
[12]	2.95 m × 3.02 m	0.0°	90.0°	3.2	1.2×10^5	7.2%	−1.4%	7.1%	40/46
[12]	2.95 m × 3.02 m	0.0°	90.0°	3.2	1.2×10^5	7.0%	−1.9%	6.7%	36/46
[12]	2.95 m × 3.02 m	0.0°	90.0°	2.0	1.9×10^5	5.3%	+0.1%	5.3%	40/46
[12]	2.95 m × 3.02 m	0.0°	90.0°	2.0	2.0×10^5	4.7%	−0.4%	4.7%	36/46
[12]	2.95 m × 3.02 m	0.0°	90.0°		2.8×10^5	4.4%	+0.5%	4.4%	40/46
[12]	2.95 m × 3.02 m	0.0°	90.0°		2.8×10^5	3.5%	+0.2%	3.5%	36/46

8.1 **Transitional and Turbulent Mixed Convection From a Vertical Square Plate.** Siebers et al. [12] measured mixed convection heat transfer from a 2.95 m × 3.02 m vertical surface at temperatures between 40 C and 600 C in horizontal flow at speeds between 1.3 m/s and 6.2 m/s. Their data table did not include ambient air properties other than temperature. Their tests were conducted in Mountain View, California; its 32 m elevation has a mean barometric pressure of 100.942 kPa and 75% mean relative humidity (and mean temperature 15.5 C).

Six of the 46 measurements had "vertical boundary layer trip wires"; those measurements were not included in the present statistics. The heated surface was smooth; its natural convection was laminar.

This investigation computes the air's kinematic viscosity ν and static thermal conductivity k at the average of the plate and ambient temperatures. Siebers et al. calculated ν and k using different effective fluid temperatures for laminar and turbulent flows.

Table 6 presents the statistics of the Siebers et al. data-set. Rows 1, 3, and 5 are computed from the 40 experiments lacking trip-wires. Rows 2, 4, and 6 also exclude four outlying measurements. The Re_c value which minimized the data-set's RMSRE (relative to measurements) was found using the "Golden section search" algorithm from Kiefer [21].

The top two rows use the $\ell^{3.2}$-norm formula $\|Re_F, Re_N\|_{3.2}$ recommended by Siebers et al. [12], but with ν and k computed at the average of the plate and ambient temperatures, as were all the rows in this investigation. The middle two rows use the ℓ^2-norm, reducing RMSRE significantly.

The bottom two rows compare the present theory with measurements. The relative error of each datum having $Re_F > 0$ is plotted in Figure 32. The relative errors versus the plate temperature are plotted in Figure 33. With the four outliers removed, present theory RMSRE is 3.5% in the bottom row of Table 6.

8.2 **Turbulent Mixed Convection.** Laminar flow along a flat plate transitions to turbulent flow starting above the critical Reynolds number Re_c. For a smooth surface, Re_c depends on the free-stream turbulence of the forced flow. The present open-intake wind-tunnel operates at wind-speeds less than 4.5 m/s ($Re < 95 \times 10^3$). While a wire screen might introduce enough turbulence to produce Re_c values this low, the 5 cm distance between the wind-tunnel's open intake and the plate would not be sufficient for that flow to become uniform.

Jaffer [18] provides an alternative. An isotropic, periodic roughness with RMS height-of-roughness ε and spatial period $L_P \ll L$ sheds rough flow when $Re > Re_\lambda = [0.664/\varepsilon]^2$. An isotropic, periodic roughness behaves as a "smooth" surface with $Re_c = L/\sqrt{\varepsilon\, L_P}$ when $Re < Re_\lambda$ and:

$$Re_c > Re_\tau = \frac{\sqrt{3}\, L}{3^3\ \varepsilon}\ \exp \frac{L_P}{3^3\ \varepsilon} \tag{48}$$

Such a flat plate engraved with a hexagonal grid of 0.5 mm deep grooves is being fabricated. Measurements from the new apparatus will be added when complete.

9. Results

Table 7 shows the Kobus and Wedekind measurements for disks whose thickness to diameter ratio is less than 0.12. The last two rows are mixed convection with fixed Ra (varying Re); the others, natural convection.

Table 8 shows measurements from the present disk apparatus ($d = 12$ mm; $t = 1$ mm) when $\psi = 90°$. Each run is at a single velocity and multiple disk temperatures.

Table 9 shows measurements from the preset disk apparatus where $\theta = 0°$.

Table 10 shows measurements from the remaining present disk orientations.

Table 7 Kobus and Wedekind [7, 15, 14] disk measurements versus present theory

Source	d	t/d	θ	ψ	RMSRE	Bias	Scatter	#
[7]	15.29 mm	0.058	0.0°		3.6%	+0.7%	3.6%	21
[7]	19.99 mm	0.069	0.0°		1.8%	−1.8%	0.4%	8
[7]	10.52 mm	0.097	0.0°		2.2%	−0.7%	2.0%	17
[14]	15.47 mm	0.063	30.0°		3.5%	−3.2%	1.6%	16
[14]	19.99 mm	0.069	30.0°		3.7%	−1.1%	3.5%	9
[14]	10.48 mm	0.090	30.0°		2.4%	−0.1%	2.4%	17
[14]	15.47 mm	0.063	60.0°		3.9%	−1.6%	3.5%	14
[14]	19.99 mm	0.069	60.0°		2.8%	−1.1%	2.6%	10
[14]	10.48 mm	0.090	60.0°		3.4%	+2.4%	2.4%	15
[15]	15.47 mm	0.063	90.0°		4.1%	−4.0%	0.6%	3
[15]	19.99 mm	0.069	90.0°		3.6%	−3.4%	1.2%	8
[15]	10.48 mm	0.090	90.0°		3.4%	−3.1%	1.5%	5
[7]	15.27 mm	0.062	0.00°	90.0°	2.7%	−0.6%	2.6%	16
[7]	19.99 mm	0.069	0.00°	0.0°	1.1%	+0.2%	1.1%	24

Table 8 Level forced flow laminar mixed convection measurements versus present theory

Source	Re_d	θ	ψ	RMSRE	Bias	Scatter	Used
present disk	1950.8	90.00°	90.00°	10.0%	−9.0%	4.2%	4/6
present disk	1540.4	90.00°	90.00°	8.6%	−5.1%	7.0%	5/6
present disk	1062.0	90.00°	90.00°	7.1%	−4.1%	5.7%	5/6
present disk	542.2	90.00°	90.00°	4.1%	−2.5%	3.2%	5/6
present disk	276.2	90.00°	90.00°	5.4%	+5.2%	1.3%	5/6
present disk	136.2	90.00°	90.00°	5.0%	+4.8%	1.1%	5/6
present disk	1990.0	82.60°	90.00°	15.5%	−1.6%	15.4%	5/6
present disk	1557.0	82.60°	90.00°	8.5%	−5.3%	6.6%	5/6
present disk	1073.4	82.60°	90.00°	7.6%	−5.9%	4.8%	5/6
present disk	548.0	82.60°	90.00°	6.5%	−6.0%	2.6%	5/6
present disk	279.8	82.60°	90.00°	1.4%	+0.6%	1.3%	5/6
present disk	137.4	82.60°	90.00°	1.7%	−0.5%	1.6%	5/6
present disk	1974.5	7.40°	90.00°	16.6%	−16.5%	1.9%	4/6
present disk	1557.2	7.40°	90.00°	13.8%	−12.7%	5.4%	5/6
present disk	1074.8	7.40°	90.00°	12.1%	−11.7%	3.2%	5/6
present disk	548.2	7.40°	90.00°	8.9%	−8.8%	1.5%	5/6
present disk	280.8	7.40°	90.00°	4.9%	−4.5%	1.9%	5/6
present disk	138.8	7.40°	90.00°	8.1%	−7.4%	3.2%	5/6
present disk	1950.2	0.00°	90.00°	9.0%	−8.9%	1.0%	4/6
present disk	1538.8	0.00°	90.00°	7.0%	−4.3%	5.6%	5/6
present disk	1061.6	0.00°	90.00°	3.9%	−3.0%	2.5%	5/6
present disk	542.2	0.00°	90.00°	1.6%	−0.3%	1.6%	5/6
present disk	276.0	0.00°	90.00°	8.1%	+6.7%	4.6%	5/6
present disk	134.6	0.00°	90.00°	4.2%	+0.0%	4.2%	5/6

The fractions in the **Used** columns indicate the number of measurements used divided by the number of measurements taken. Disk temperatures less than 36.5 C were not used because they were not within the calibrated temperature range of the disk.

Table 9 Vertical disk laminar mixed convection measurements versus present theory

Source	Re_d	θ	ψ	**RMSRE**	**Bias**	**Scatter**	**Used**
present disk	1963.8	0.00°	180.00°	12.5%	−11.2%	5.6%	5/6
present disk	1539.2	0.00°	180.00°	12.4%	−11.9%	3.5%	5/6
present disk	1061.8	0.00°	180.00°	15.3%	−15.1%	2.8%	5/6
present disk	541.8	0.00°	180.00°	16.8%	−16.5%	3.4%	5/6
present disk	273.6	0.00°	180.00°	14.0%	−11.5%	8.1%	5/6
present disk	191.8	0.00°	180.00°	18.8%	−16.1%	9.8%	5/6
present disk	161.0	0.00°	180.00°	21.4%	−19.8%	8.1%	5/6
present disk	135.8	0.00°	180.00°	23.5%	−20.9%	10.8%	6/6
present disk	112.3	0.00°	180.00°	21.2%	−20.2%	6.6%	6/6
present disk	94.2	0.00°	180.00°	25.4%	−24.6%	6.1%	6/6
present disk	1965.8	0.00°	173.30°	5.8%	−3.1%	4.9%	5/6
present disk	1540.8	0.00°	173.30°	5.9%	−3.6%	4.6%	5/6
present disk	1063.2	0.00°	173.30°	6.4%	−5.7%	2.8%	5/6
present disk	542.4	0.00°	173.30°	5.9%	−4.2%	4.2%	5/6
present disk	273.8	0.00°	173.30°	8.7%	+4.0%	7.8%	5/6
present disk	192.6	0.00°	173.30°	10.4%	+0.7%	10.4%	5/6
present disk	161.4	0.00°	173.30°	11.3%	+1.2%	11.2%	5/6
present disk	134.6	0.00°	173.30°	13.6%	+0.5%	13.6%	5/6
present disk	112.3	0.00°	173.30°	8.4%	+7.1%	4.5%	6/6
present disk	94.8	0.00°	173.30°	7.5%	−3.4%	6.7%	6/6
present disk	1978.2	0.00°	96.80°	4.4%	−3.6%	2.5%	4/6
present disk	1560.4	0.00°	96.80°	5.9%	+3.2%	4.9%	5/6
present disk	1076.6	0.00°	96.80°	6.9%	+6.6%	2.1%	5/6
present disk	549.6	0.00°	96.80°	12.6%	+12.4%	2.2%	5/6
present disk	279.2	0.00°	96.80°	21.4%	+21.0%	4.0%	5/6
present disk	137.2	0.00°	96.80°	18.0%	+17.6%	3.3%	5/6
present disk	1947.0	0.00°	82.30°	11.7%	−1.2%	11.6%	5/6
present disk	1525.0	0.00°	82.30°	6.2%	−3.0%	5.5%	5/6
present disk	1051.6	0.00°	82.30°	2.5%	+0.7%	2.4%	5/6
present disk	536.6	0.00°	82.30°	12.1%	+11.8%	2.3%	5/6
present disk	273.2	0.00°	82.30°	20.8%	+20.3%	4.2%	5/6
present disk	133.4	0.00°	82.30°	10.9%	+9.6%	5.2%	5/6
present disk	1966.0	0.00°	7.71°	13.2%	−11.2%	7.0%	5/6
present disk	1521.0	0.00°	7.71°	13.1%	−13.0%	2.2%	5/6
present disk	1049.2	0.00°	7.71°	10.1%	−9.9%	1.8%	5/6
present disk	535.4	0.00°	7.71°	4.6%	+2.0%	4.2%	5/6
present disk	273.3	0.00°	7.71°	14.2%	+13.7%	3.6%	6/6
present disk	138.3	0.00°	7.71°	3.8%	+2.8%	2.6%	6/6
present disk	92.7	0.00°	7.71°	12.2%	−11.8%	3.1%	6/6
present disk	1970.0	0.00°	0.00°	9.0%	−6.8%	6.0%	5/6
present disk	1544.0	0.00°	0.00°	6.8%	−5.4%	4.1%	5/6
present disk	1065.2	0.00°	0.00°	5.2%	−4.8%	1.9%	5/6
present disk	543.4	0.00°	0.00°	4.0%	+2.8%	2.8%	5/6
present disk	275.2	0.00°	0.00°	14.8%	+14.5%	3.2%	5/6
present disk	139.8	0.00°	0.00°	5.3%	+4.7%	2.5%	5/6

Table 10 Inclined disk laminar mixed convection measurements versus present theory

Source	Re_d	θ	ψ	RMSRE	Bias	Scatter	Used
present disk	1968.2	6.65°	173.30°	24.1%	−23.5%	5.4%	5/6
present disk	1541.6	6.65°	173.30°	26.4%	−26.1%	3.9%	5/6
present disk	1063.6	6.65°	173.30°	32.0%	−31.9%	2.1%	5/6
present disk	542.6	6.65°	173.30°	34.1%	−33.5%	6.1%	5/6
present disk	275.0	6.65°	173.30°	31.8%	−30.6%	8.5%	5/6
present disk	192.6	6.65°	173.30°	38.3%	−36.4%	11.9%	5/6
present disk	162.2	6.65°	173.30°	40.3%	−38.3%	12.6%	5/6
present disk	135.2	6.65°	173.30°	46.1%	−43.9%	13.9%	5/6
present disk	114.2	6.65°	173.30°	38.3%	−37.7%	6.8%	6/6
present disk	94.7	6.65°	173.30°	43.5%	−42.8%	7.8%	6/6
present disk	1989.2	81.50°	98.50°	17.6%	−1.0%	17.6%	5/6
present disk	1556.4	81.50°	98.50°	8.4%	−4.7%	7.0%	5/6
present disk	1073.6	81.50°	98.50°	8.0%	−6.6%	4.6%	5/6
present disk	548.2	81.50°	98.50°	5.1%	−4.5%	2.3%	5/6
present disk	278.8	81.50°	98.50°	5.0%	+4.9%	1.2%	5/6
present disk	136.0	81.50°	98.50°	5.9%	+5.8%	1.3%	5/6
present disk	1936.4	82.30°	82.30°	10.2%	−6.8%	7.6%	5/6
present disk	1517.0	82.30°	82.30°	8.7%	−6.0%	6.3%	5/6
present disk	1046.4	82.30°	82.30°	7.3%	−5.9%	4.2%	5/6
present disk	534.2	82.30°	82.30°	4.4%	−4.2%	1.5%	5/6
present disk	272.4	82.30°	82.30°	5.9%	+5.7%	1.6%	5/6
present disk	132.2	82.30°	82.30°	4.7%	+4.2%	2.1%	5/6
present disk	1958.6	7.71°	7.71°	27.6%	−27.5%	1.5%	5/6
present disk	1534.8	7.71°	7.71°	24.8%	−24.7%	0.9%	5/6
present disk	1058.2	7.71°	7.71°	21.8%	−21.7%	1.7%	5/6
present disk	540.2	7.71°	7.71°	12.5%	−11.9%	3.7%	5/6
present disk	273.6	7.71°	7.71°	3.3%	+1.7%	2.8%	5/6
present disk	139.3	7.71°	7.71°	7.9%	−7.6%	2.1%	6/6
present disk	93.2	7.71°	7.71°	19.3%	−19.1%	3.1%	6/6

Table 11 Laminar–turbulent transitional mixed convection versus present theory

Source	Dimensions	θ	ψ	Re_c	RMSRE	Bias	Scatter	Used
[12]	2.95 m × 3.02 m	0.0°	90.0°	2.8×10^5	4.4%	+0.5%	4.4%	40/46
[12]	2.95 m × 3.02 m	0.0°	90.0°	2.8×10^5	3.5%	+0.2%	3.5%	36/46

Table 11 shows laminar–turbulent transitional mixed convection measurements from Siebers et al. [12]

10. Discussion

This investigation completes the series of four articles (Jaffer [4], Jaffer [18], Jaffer and Jaffer [16], and the present work) addressing external convection from a rough or smooth, flat, isothermal surface.

The present work's core advance is Formulas (34–37) describing mixed convection along a smooth vertical plate with $0° \le \psi \le 180°$.

10.1 **Application.** Predicting the convective heat transfer to and from exterior walls is crucial in correctly sizing the cooling and heating systems of buildings. In combination with the rough-surface mixed convection work Jaffer and Jaffer [16], the formulas derived in the present work provide a practically complete engineering model of convective heat transfer of flat walls and roofs, both rough and smooth.

10.2 **Disks.** Developed in order to test laminar flow measurements, the whole-disk model is incomplete in that it is accurate only for thin ($t/d < 0.12$) disks and laminar flows.

10.3 **Cylinders.** Developed for the present apparatus, the cylinder mixed convection model in Section 13 is incomplete in that it requires forced flow to be perpendicular to the cylinder and was only tested at $Re_f < 500$. Even with those restrictions, it may find application to cooling fins.

10.4 **Methodology.** Although the ℓ^p-norm has been used in prior work convection formulas, it is used quite extensively through these four articles. Nested exponential coefficients and p functions may be unprecedented, but are very successful in modeling transitional behavior with continuously differentiable expressions.

11. Conclusions

A set of formulas was proposed for predicting the average mixed convective conductance of an isothermal flat plate with convex perimeter subjected to a uniform forced flow parallel to its surface.

These formulas were tested with 574 heat transfer measurements in 101 data-sets at 14 orientations from 3 peer-reviewed studies, a Sandia National Laboratories technical report, and the present apparatus. Compared with the present theory, the 101 root-mean-squared relative error values span 0.8% through 5.1%.

Supplementary Materials

A zip archive of PDF files containing graphs and estimated measurement uncertainties of the disk convection measurements in each orientation can be downloaded from:

`https://people.csail.mit.edu/jaffer/convect`

Acknowledgments

Thanks to Carl Mikkelsen for fabricating the disk holder, machining the plate, and excellent suggestions.

12. **Nomenclature**

$A_\bullet, A_\circ$	area of disk's face, rim (m^2)
d	disk diameter (m)
$\overline{h}$	average convective surface conductance ($W/(m^2 \cdot K)$)
$\overline{h_F}$	forced convective surface conductance ($W/(m^2 \cdot K)$)
$\overline{h^*}$	upward natural convective surface conductance ($W/(m^2 \cdot K)$)
$\overline{h'}$	vertical plate natural convective surface conductance ($W/(m^2 \cdot K)$)
$\overline{h_R}$	downward natural convective surface conductance ($W/(m^2 \cdot K)$)
k	fluid thermal conductivity ($W/(m \cdot K)$)
L	characteristic length (m)
L_P	roughness spatial period (m)
L^*	natural characteristic length of upward-facing surface (m)
$L^*_\cap$	natural characteristic length of top 1/4 of vertical disk rim (m)
$L'_\mid$	natural characteristic length of side 1/4 of vertical disk rim (m)
L'	natural characteristic length of vertical surface (m)
L_R	natural characteristic length of downward-facing surface (m)
$L_\cup$	natural characteristic length of bottom 1/4 of vertical disk rim (m)
Nu'_0	Nusselt number of vertical plate conduction
Nu^*_0	Nusselt number of upward-facing plate conduction
$\overline{Nu}$	average Nusselt number
$\overline{Nu^*}$	average Nusselt number of upward-facing natural convection
$\overline{Nu'}$	average Nusselt number of vertical plate natural convection
$\overline{Nu_R}$	average Nusselt number of downward-facing natural convection
$\overline{Nu_\sigma}$	average Nusselt number of forced convection
$\overline{Nu_\lambda}$	average Nusselt number of laminar forced convection
$\overline{Nu_\tau}$	average Nusselt number of turbulent forced convection
$\overline{Nu_\circ}$	average Nusselt number of cylinder forced convection
p	exponent in ℓ^p-norm
p^*	exponent in ℓ^p-norm for an upward-facing plate
Pr	Prandtl number of the fluid
Ra	Rayleigh number
Ra_d	Rayleigh number with disk diameter as characteristic length
Ra^*	upward Rayleigh number with characteristic length L^*
$Ra^*_\cap$	upward 1/4 rim Ra with characteristic length $L^*_\cap$
Ra'	vertical plate Rayleigh number with characteristic length L'
$Ra'_\mid$	vertical 1/4 rim Ra with characteristic length $L'_\mid$
Ra_R	downward Rayleigh number with characteristic length L_R
$Ra_\cup$	bottom 1/4 rim Ra with characteristic length $L_\cup$
Re	Reynolds number
Re_0	laminar Re constant; $Re_0 \approx 600$
Re_c	critical Reynolds number; maximum smooth purely laminar Re_F
Re_d	Reynolds number with disk diameter d as characteristic length
Re_F	Reynolds number of the forced flow parallel to the plate
Re_N	effective Reynolds number of vertical natural convection
$Re_{N/2}$	effective Reynolds number of 1/2 vertical natural convection
Re_λ	Re_F where laminar momentum boundary layer $\delta_2 = \varepsilon$
Re_τ	Re_F where turbulent momentum boundary layer $\delta_2 = \varepsilon$
$S_\circ$	disk rim shape factor
t	thickness of disk (m)
$u(y)$	velocity at distance y from the height mid-line of a vertical plate (m/s)
u_F	bulk forced flow velocity (m/s)
u_N	effective natural flow speed $= \nu\, Re_N/L$ (m/s)
$\overline{U_F}$	forced thermal conductance of vertical disk's face (W/K)

$\overline{U_N}$	natural thermal conductance of inclined disk (W/K)
$\overline{U_\bullet}$	forced thermal conductance of disk face (W/K)
$\overline{U_\circ}$	forced thermal conductance of disk rim (W/K)
$\overline{U_=}$	natural thermal conductance of horizontal disk rim (W/K)
$\overline{U^*}$	natural thermal conductance of horizontal disk's upper face (W/K)
$\overline{U_R}$	natural thermal conductance of horizontal disk's lower face (W/K)
$\overline{U_\cap}$	natural thermal conductance of top quarter of disk rim (W/K)
$\overline{U_\mid}$	natural thermal conductance of side quarter of disk rim (W/K)
$\overline{U_\cup}$	natural thermal conductance of bottom quarter of disk rim (W/K)
$\overline{U_\uparrow}$	mixed thermal conductance of upper face of horizontal disk (W/K)
$\overline{U_\downarrow}$	mixed thermal conductance of lower face of horizontal disk (W/K)
$\overline{U_\parallel}$	mixed thermal conductance of vertical disk rim (W/K)
y	normal distance from the plate (m)

12.1 **Greek Symbols.**

δ	boundary layer thickness (m)
δ_λ	laminar boundary layer thickness (m)
δ_τ	turbulent boundary layer thickness (m)
δ_2	momentum boundary layer thickness (m)
ε	surface RMS height-of-roughness (m)
η	turbulent Re_F correction coefficient
γ, γ'	exponent p of the ℓ^p-norm
Ω	unit of electrical resistance
ν	fluid kinematic viscosity (m^2/s)
Φ	vertical disk reuptake coefficient
ψ	angle between forced flow and the zenith; 0° is aiding; 180° is opposing
θ	angle of the plate surface from vertical; face up is −90°; face down is +90°
Ξ	natural convection self-obstruction factor
ζ	vertical Re_F correction coefficient

12.2 **Abbreviations.** The following abbreviations are used in this manuscript:

RMS	root-mean-squared $\sqrt{\sum_{i=1}^{n} x_i^2/n}$
RMSRE	root-mean-squared relative error (%)

13. Appendix A: Disk Apparatus and Measurement Methodology

The wind-tunnel and electronics described in Jaffer [18] were adapted for the present work. The suspended 0.305 m square plate was replaced by a TDK B59060A0040A010, a 12 mm diameter, 1 mm thick positive temperature coefficient resistor (thermistor) disk similar to those employed by Kobus and Wedekind [7].

The electrical resistance of thermistor material increases with temperature, allowing the electrical current which heats the disk to also measure its electrical resistance, hence its temperature. When a current flows through the thermistor, regions with lower resistance receive more current, leading to heating and uniform temperature of the disk.

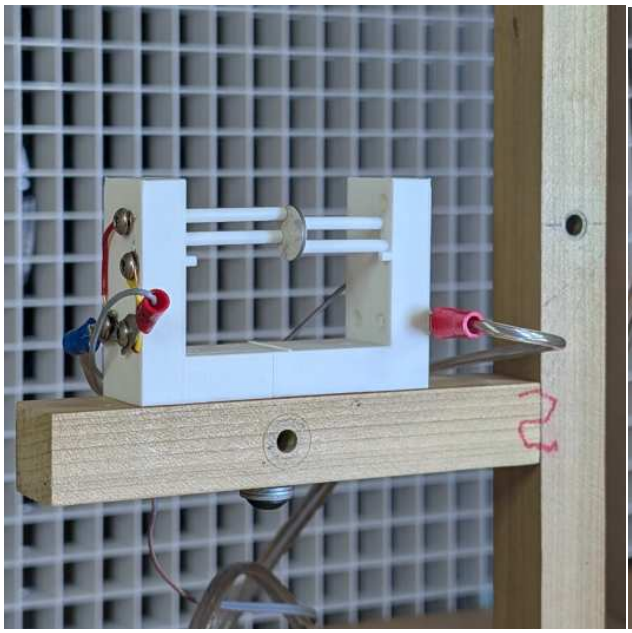

Figure 34 Vertical disk

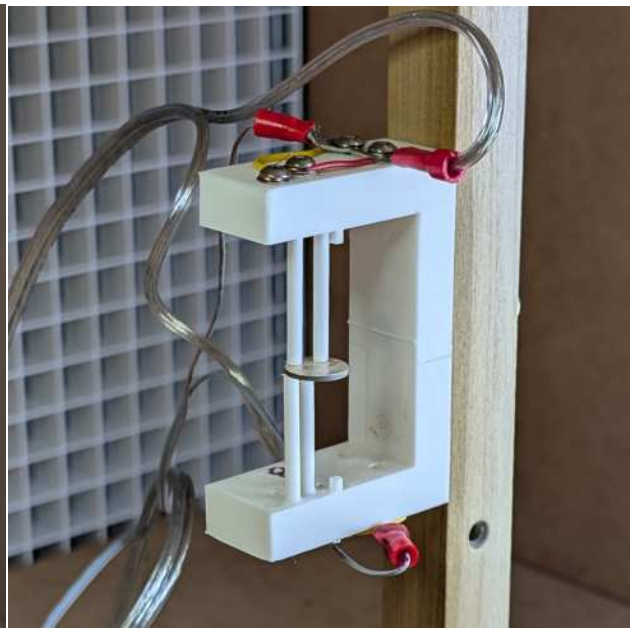

Figure 35 Horizontal disk

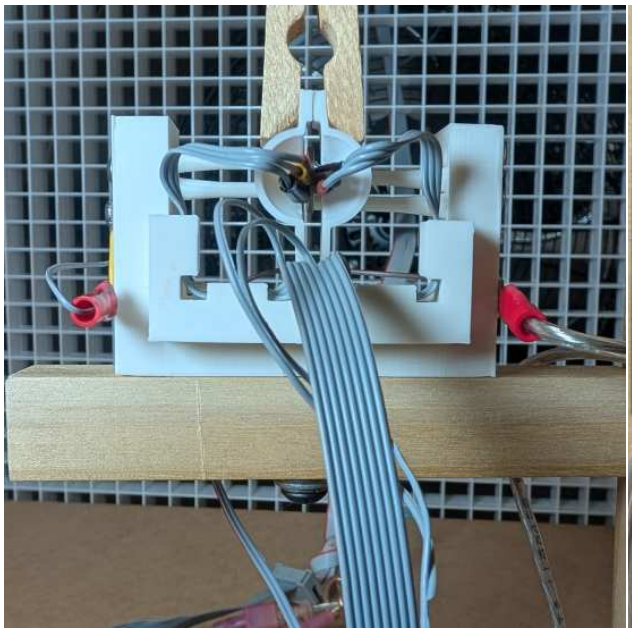

Figure 36 Disk calibration front

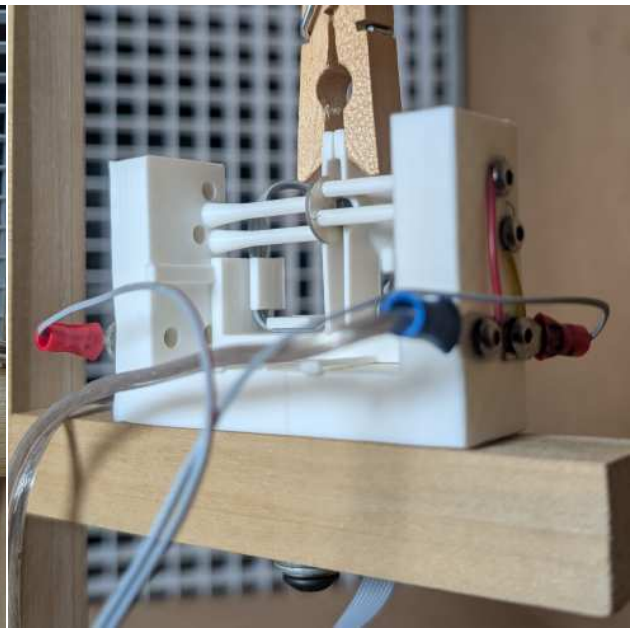

Figure 37 Disk calibration back

Figures 34 and Figures 35 show the 12 mm thermistor disk in vertical and horizontal fixtures, respectively. The white acrylonitrile butadiene styrene (ABS) fixture holds the disk with four 2.8 mm diameter tubes. A 0.2 mm diameter Constantan wire threads each tube and folds over the tube end, making electrical

connection to the silvered surface of the disk. The electrical current to heat the disk flows through a pair of wires on opposite sides of the disk. The other pair of wires measures the voltage across the disk. The disk's electrical resistance is this voltage divided by the current flowing through the disk.

The thermistor resistance is a non-linear function of its temperature, and varies widely between disks. Temperature calibration is thus specific to each disk.

Figures 36 and 37 show a calibration fixture snapped into the disk holder. A clothespin clamps the fixture, holding LM37 temperature sensors against each side of the disk.

Figure 38 shows temperatures T_1 and T_2 measured by the LM37s, along with electrical resistance $R = E/I$ and temperature $T(R)$ calculated from the thermistor current I and voltage E.

A formula was fitted to the measurements as shown in Figure 38. RMSRE was computed from $\Delta T = T - 20$ C of the last ten readings at each temperature plateau cooler than 60 C; this reflects the ΔT sensitivity of Ra in heat transfer calculations. The RMSRE of this formula relative to the average of the LM37s was less than 0.1% between 38 C and 58 C with $T_\infty \approx 18$ C. In order to avoid a bias in measurements, rising and falling LM37 temperatures were averaged as shown in Figure 39. Figure 40 shows the resulting temperature curve relative to the disk's electrical resistance. With the fan running, disk temperatures as low as 35 C were captured, significantly lower than the calibrated range; measurements of temperatures below 36.5 C were not used in the present data sets.

Figure 41 shows $T(R)$ without the LM37s attached; while similar to Figure 38, less power P ($= E\,I$) is required to maintain temperature of the disk. Figure 41 has six temperature levels between 35 C and 60 C.

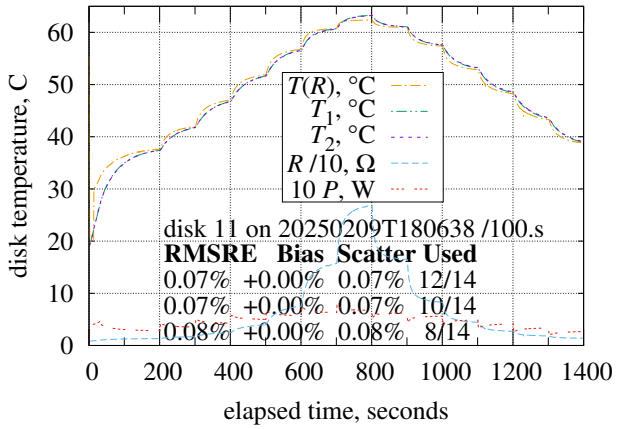

Figure 38 Disk with calibration chips

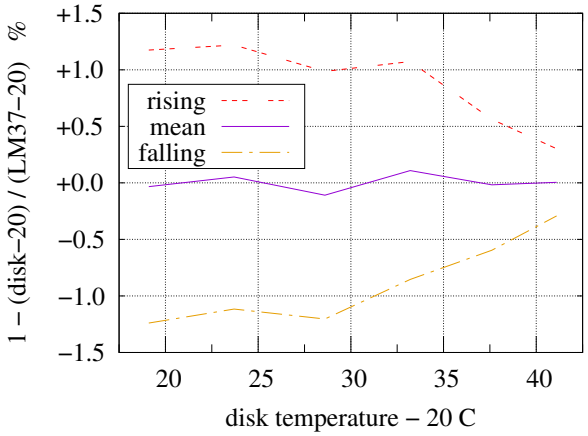

Figure 39 Temperature relative error

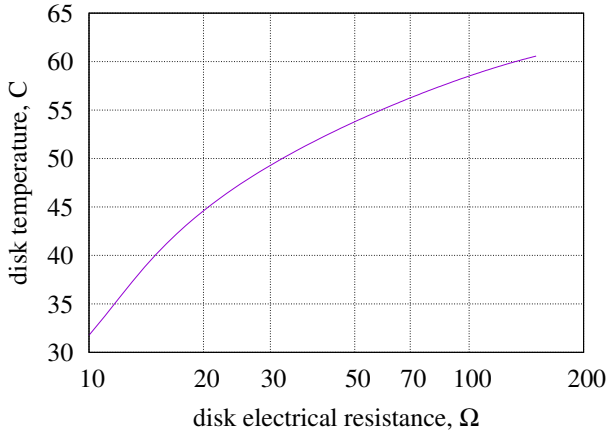

Figure 40 Disk temperature curve

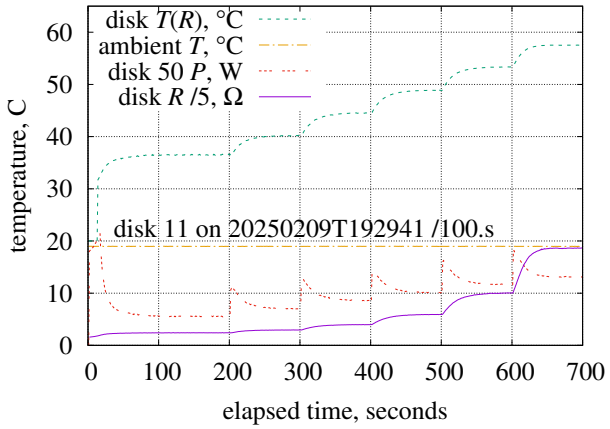

Figure 41 Disk alone

The thermistor disk in the present apparatus is held in place by four thin tubes which are always perpendicular to the disk (and to the forced airflow). Thus, while θ is the disk's angle from vertical, θ is the tube's angle from horizontal.

13.1 **Natural Convection Heat Transfer From an Inclined Cylinder.** Formulas (49) and (50) model horizontal and vertical cylinders, respectively.

$$\overline{h^\bullet} = \frac{k}{d} \left\| \frac{Nu_0^\bullet}{2} \ , \ \sqrt[2+E^\bullet]{\left[\frac{\pi\, Nu_0^\bullet}{6}\right]^{3+E^\bullet} \frac{Ra_d}{\pi\, \Xi_\bullet}} \right\|_{1/3} \approx \frac{k}{d} \left\| 0.177 \ , \ 0.118 \left[\frac{Ra_d}{\Xi_\bullet}\right]^{0.310} \right\|_{1/3} \tag{49}$$

$$\overline{h^\parallel} = \frac{k}{H} \left\| \frac{Nu_0^\bullet}{2} \frac{H}{d} \ , \ \sqrt[3]{\left[\frac{Nu_0^\bullet}{12}\right]^4 \frac{d}{H} \frac{2\, Ra_H}{\Xi}} \right\|_{1/6} \approx \frac{k}{H} \left\| 0.177 \frac{H}{d} \ , \ 0.0115 \sqrt[3]{\frac{d}{H} \frac{Ra_H}{\Xi}} \right\|_{1/6} \tag{50}$$

$$Nu_0^\bullet = 2^{-3/2} \approx 0.354 \tag{51}$$

$$\Xi_\bullet = \left\| 1 \ , \ \frac{\sqrt{1/3}}{Pr} \right\|_{\sqrt{1/3}} \qquad \Xi = \left\| 1 \ , \ \frac{1/2}{Pr} \right\|_{\sqrt{1/3}} \tag{52}$$

$$E^\bullet = \frac{5}{6} + \frac{11}{9\,\pi} \approx 1.222 \tag{53}$$

Figure 42 graphs Formula (50) and Formula (49).

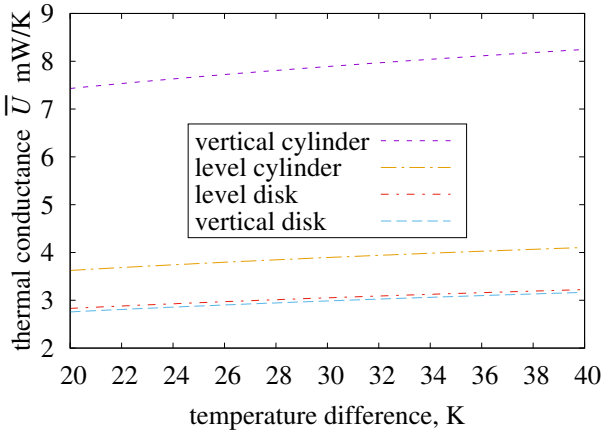

Figure 42 Natural convections from cylinder and disk in air

ϑ is the angle of a cylinder's axis from horizontal.

Flow along a flat surface is strongly constrained by that surface; competing flows combine with the ℓ^{16}-norm ($p = 16$). Flows around an inclined cylinder are less constrained but still compete, suggesting a smaller $p > 1$.

However, natural convection flows around a long thin cylinder will be more competitive ($p \gg 1$) than from a cylinder where $H \approx d$. This suggests combining $\overline{h^\parallel}$ and $\overline{h^\bullet}$ with $p = 1 + H/d$:

$$\overline{U} = \pi\, d\, H \left\| \overline{h^\parallel}\,(|\sin\vartheta|\, Ra_H),\ \overline{h^\bullet}\,(|\cos\vartheta|\, Ra_d) \right\|_{1+H/d} \tag{54}$$

13.2 **Heat Transfer From a Non-Isothermal Cylinder.** ABS cylinders and ABS tubes threaded by Constantan wire ($k_W \approx 20\mathrm{W}/(\mathrm{m}\cdot\mathrm{K})$) are not isothermal.

It is common practice to model lumped element heat transfer problems as electrical circuits where electrical current is replaced by heat transfer, and voltage is replaced by temperature difference ΔT. Similarly, distributed element heat transfer problems can be modeled as electrical transmission lines, reducing them to equivalent lumped element conductances in many cases. Doing so can facilitate a more intuitive understanding than the partial differential equations underlying both models.

This investigation uses transmission line theory to parlay convective conductances of an isothermal cylinder into conductances of a cylinder which is not isothermal. Although natural convective conductances

are not linear in ΔT, the thermal resistance along the cylinder attenuates the contributions of convective conductances away from its heated end.

Consider the heated end of a cylinder. Each $\mathrm{d}L$ slice transfers heat to the fluid with convective conductance per unit length $U_{\mathrm{d}L} = k_f\,\pi\,\overline{Nu}/\mathrm{d}L$, but also resists heat flow to the rest of the cylinder with resistance per unit length $R_{\mathrm{d}L} = \mathrm{d}L/[k_{\mathrm{ABS}}\,A_\times\,\mathrm{d}L] = 1/[k_{\mathrm{ABS}}\,A_\times]$, where $k_{\mathrm{ABS}} \approx 179$ mW/(m · K) is the thermal conductivity of the cylinder and $A_\times$ is its cross-sectional area. Transmission line theory suggests that the convective conductance from the heated end of an infinitely long cylinder is the square-root of the conductance–resistance ratio, $\sqrt{U_{\mathrm{d}L}/R_{\mathrm{d}L}}$. When the unheated end of a length l cylinder is held at ambient temperature:

$$\frac{\sqrt{U_{\mathrm{d}L}/R_{\mathrm{d}L}}}{\tanh\left(l\,\sqrt{U_{\mathrm{d}L}\,R_{\mathrm{d}L}}\right)} \tag{55}$$

The tubes in the present apparatus are more complicated than a solid cylinder. In assembling the disk holder, a 0.188 mm Constantan wire was pushed through the 1.11 mm hole in each 25 mm long tube. The effective thermal resistance per length along the tube (and wire) is:

$$\frac{4/\pi}{k_{\mathrm{ABS}}\,[D_O^2 - D_I^2] + k\,[D_I^2 - D_W^2] + k_W\,D_W^2} \approx 656 \times 10^3\ \frac{\mathrm{K}}{\mathrm{W}\cdot\mathrm{m}} \tag{56}$$

Per length, the ABS tube thermal conductance is 66% larger than the wire conductance. The still air longitudinal conductance is negligible.

The per length radial conductance from the inside surface to the outside surface of a tube is:

$$\frac{2\,\pi\,k_{\mathrm{ABS}}}{\ln(D_O/D_I)} \approx 1.21\frac{\mathrm{W}}{\mathrm{K}\cdot\mathrm{m}} \tag{57}$$

. where D_I and D_O are the tube's inner and outer diameters, respectively.

But heat flows within the tube wall, leading to an increase in radial conduction which grows with D_O/D_I. This is modeled by expanding the inner diameter from D_I to the geometric mean diameter $\sqrt{D_I\,D_O}$:

$$\frac{2\,\pi\,k_{\mathrm{ABS}}}{\ln(D_O/\sqrt{D_I\,D_O})} = \frac{4\,\pi\,k_{\mathrm{ABS}}}{\ln(D_O/D_I)} \approx 2.42\frac{\mathrm{W}}{\mathrm{K}\cdot\mathrm{m}} \tag{58}$$

.

The Constantan wire does not fill the tube's axial hole and is not concentric with it, limiting the analysis. Its effect on radial conductance is modeled by substituting $D_i = 0.9\,D_I$ for D_I; this reduces the radial conductance 10% to 2.17 W/(K · m).

With black-body radiative surface conductivity h_{BB}, wind-tunnel emissivity ϵ_{wt}, and tube emissivity $\epsilon_{ABS} \approx 0.92$, the effective surface conductance per length is:

$$\left\| \frac{4\,\pi\,k_{\mathrm{ABS}}}{\ln(D_O/D_i)},\ U_{\mathrm{d}L} + \pi\,D_O\,\epsilon_{ABS}\,\epsilon_{wt}\,h_{BB} \right\|_{-1} \tag{59}$$

The temperature difference from ambient decreases along the tube from its heated end. It decreases to $\exp(-1) \approx 0.368$ of ΔT at distance $1/\sqrt{U_{\mathrm{d}L}\,R_{\mathrm{d}L}}$. In natural convection this distance is about 2.7 mm for a vertical tube and 2.5 mm for a horizontal tube. With 2.73 m/s airflow this distance decreases to 1.5 mm.

13.3 **Constantan Wires.** The Constantan wire pinched between the disk and the ABS tube end has thermal conductance 18.2 mW/K; including the disk–tube air gap raises the conductance to 19.0 mW/K.

The electrical current I flowing through the thermistor disk also flows through two of the Constantan wires. Each wire dissipates $I^2\,R$, where $R \approx 0.575\ \Omega$ is the electrical resistance of one Constantan lead wire.

13.4 **Disk-Tube Reuptake.** Fluid heated by the disk can impede convective heat transfer from the tubes. In other orientations, fluid heated by the tubes can impede convective heat transfer from the disk.

In Section 7 the reuptake coefficients between the rim and faces of a disk are functions of only the disk's geometry and orientation. This is not the case for reuptake between the disk and tubes.

If the disk and tube natural convective conductance formulas are close to correct, then the natural disk-tube reuptake coefficient be calculated as the difference between the predicted total heat transfer (without disk-tube reuptake) and the measured heat transfer divided by the predicted disk's heat transfer. Note that valid reuptake coefficients must be bounded by 0 and 1.

Reuptake calculations do not corrupt the 12 mm disk rows in Section 9 because only $Re_d > 0$ results are reported there, and the disk-tube reuptake coefficients are calculated only with $Re_d = 0$.

Mixed convection disk-tube reuptake coefficients vary with Re_d. Fortunately, they can be calculated from the natural convection reuptake coefficients measured in the same orientation.

Natural convection measurements at multiple temperatures were made at twenty-five angles between 0° and 180°. The "reuptake coefficient" (using the right side scale) in Figure 44 shows the values so calculated.

Using a reuptake coefficient computed for each orientation, Figure 43 shows that reuptake coefficients are not significantly dependent on disk temperature; RMSRE values are less than 0.5% at all twenty-five angles tested. However, reuptake coefficient varies with ambient temperature. To minimize ambient variations, each orientation's measurements per fan speed were performed consecutively; the natural reuptake coefficient used was taken from natural convection measurements at the start or end of an orientation's data set. Many mixed convection data-sets were spoiled by ambient changes during the run.

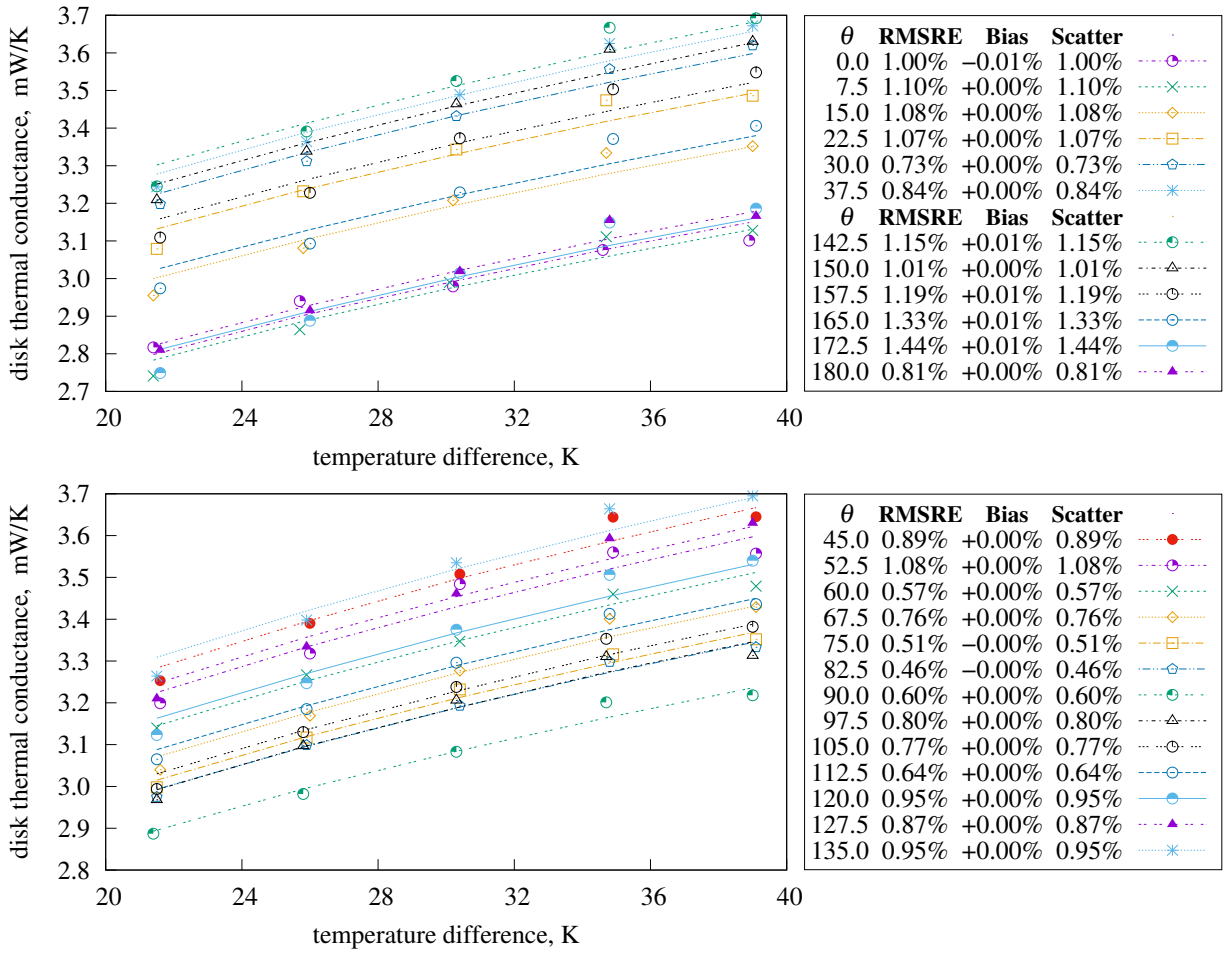

Figure 43 Disk natural convection versus ΔT by θ

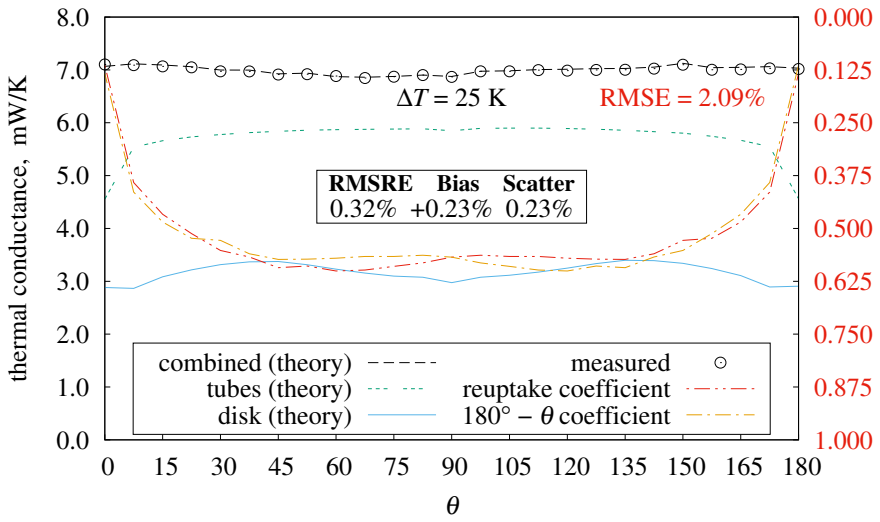

Figure 44 Disk natural convection versus θ

The reuptake fractions being larger than 70% is explained by the tube heating from the disk being confined within a few millimeters $(1/\sqrt{U_{dL}\,R_{dL}})$ of the tube's hot end.

The "$180° - \theta$ coefficient" trace is the same as "reuptake coefficient", but with the angles reversed. The RMSRE between these traces is less than 1.7%, indicating a rough equivalence between natural convection reuptake coefficient when the disk is lower than the tubes (Figure 45(a)) versus higher (Figure 45(b)).

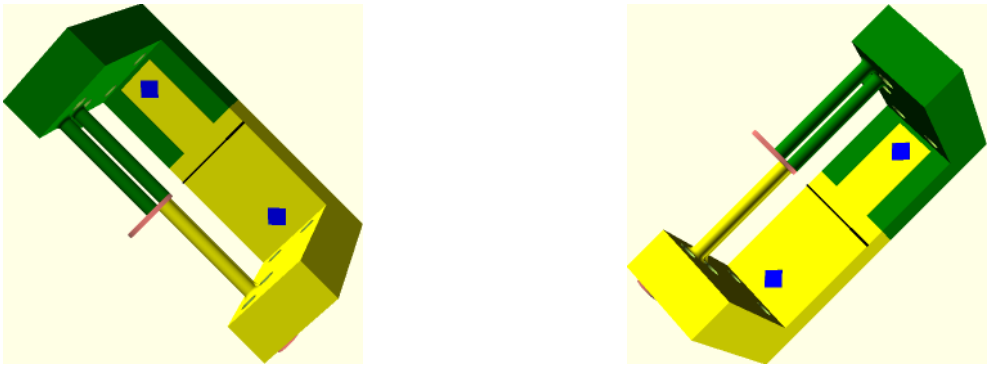

a **b**

Figure 45 Fixture (a) $\theta = 45°$ (b) $\theta = 135°$

13.5 **Mixed Convection From a Cylinder.** From $\overline{Nu_\circ}$ Formula (42), the forced convective heat transfer across a cylinder $\overline{U_f} = k\,\pi\,l\,D\,\overline{Nu_\circ}/D = \pi\,k\,l\,\overline{Nu_\circ}$.

As with a flat surface, natural convection cannot be entirely canceled by opposing forced convection. However, without the detailed understanding of cylinder boundary layers, the Re approach of Section 6 is not feasible. Instead, this investigation uses the ℓ^p-norm to combine $\overline{U_f}$ and $\overline{U_n}$, the cylinder forced (perpendicular to the cylinder) and natural convection components, respectively. Natural convection and level forced flow apparently combine using the same $p_/ = 2^3/\sqrt[4]{2} \approx 6.727$ as horizontal and vertical natural convections combine with. Opposing flows should combine as $\|\overline{U_n}\ ,\ \overline{U_f}\|_{p_+}$ reduced by an amount related to the smaller of $\overline{U_n}$ and $\overline{U_f}$. Recalling from Section 1, when $p < 0$, then $\|F_1, F_2\|_p \le \min(|F_1|, |F_2|)$. Thus the reduction should be proportional to $\|\overline{U_n}\ ,\ \overline{U_f}\|_{p_-}$, where $1 < p_+ < p_/$ and $-p_/^2 < p_- < -1$ depend on Re_f and ψ. Proposed is the mixed convection for an isothermal cylinder:

$$\left\|\overline{U_n}\ ,\ \overline{U_f}\right\|_{p_+} - \cos^2\psi \sqrt{\frac{\|1,1\|_{p_+}}{\|b_n, b_f\|_{p_-}}}\ \left\|\overline{U_n}\,b_n\ ,\ \overline{U_f}\,b_f\right\|_{p_-} \tag{60}$$

$$p_- = -\left[\frac{p_/}{p_+}\right]^2 \qquad b_n = \exp_{1/2}\left(\frac{p_+^2}{4}\right) \qquad b_f = \sqrt[4]{1/b_n} \tag{61}$$

Note that heat transfer is subtracted in both aiding and opposed flows. It is unlikely that the minimum will occur at $\overline{U_n} = \overline{U_f}$; hence coefficients $0 < b_n \leq 1$ and $b_f \geq 1$ scale $\overline{U_n}$ and $\overline{U_f}$. The square-root factor in Formula (60) scales the subtracted thermal conductance $\| \overline{U_n}\, b_n \ , \ \overline{U_f}\, b_f \|_{p_-}$ to be commensurate with $\|\overline{U_n} \ , \ \overline{U_f}\|_{p_+}$.

The Figure 46 drawings show the Stokes (creeping) forced flow component in aiding, horizontal, and opposing flow cases. In the opposing and horizontal flow cases, Stokes flow and natural convection will compete for cylinder area when $Re_f < 5$; thus $p > 3$ at $Re_f < 5$. The natural and aiding Stokes flow convections simply add with $p \approx 1$.

The Figure 47 drawings show the laminar forced flow regime at $5 < Re_f < 40$ in the aiding, horizontal, and opposing flow cases. In the (left) aiding case, the flows also combine with $p \approx 1$. In the (right) opposing case the induced vortex flows are compatible with the natural flow; their $p \approx 1$. The (center) horizontal flow case is competitive with $p > 3$.

At $Re_f > 60$ the vortexes alternately detach and regenerate, forming a "Kármán vortex street". When laminar, this regime is additive with $p \approx 1$. Vertical forced flows, already having transitioned to $p = 1$, have no transition. Level forced flow transitions around $Re_f \approx 60$.

According to Lienhard and Lienhard [20] (p. 386), the level forced flow transition to vortex turbulence occurs $150 < Re_f < 300$. Turbulent flow can't combine with natural flow as $p = 1$. In aiding flow, the lower half of the cylinder having a thinner natural boundary layer than the other orientations lowers its transition to $Re_f \approx 90$. Opposing and level forced flows transition around $Re_f \approx 300$.

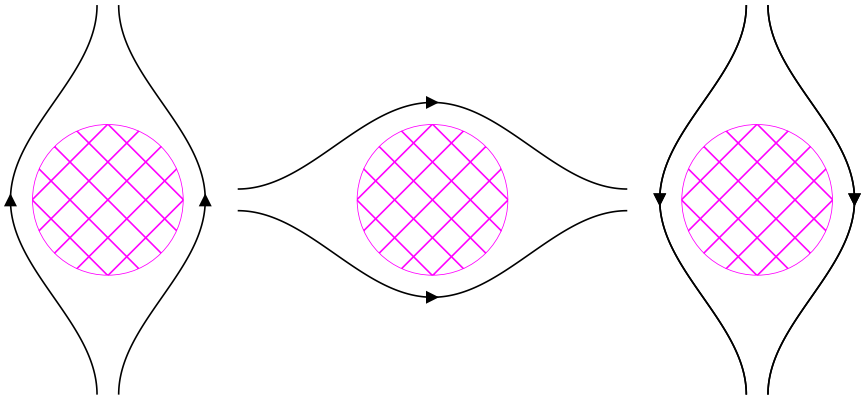

Figure 46 **Stokes flow around cylinder** $Re_f < 5$

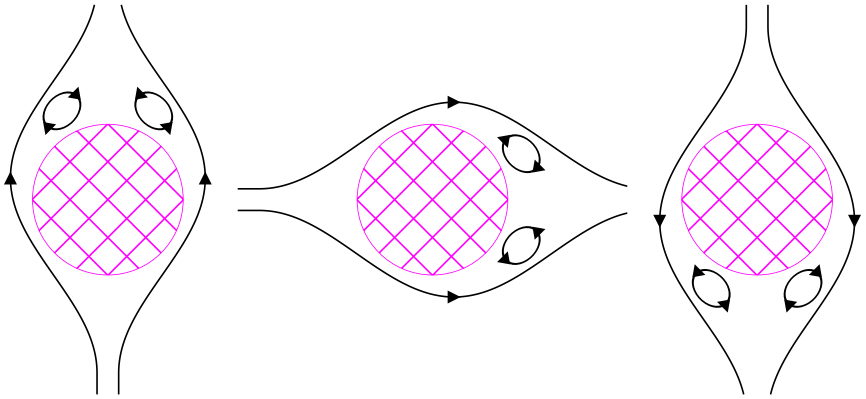

Figure 47 **Foppl vortexes from cylinder** $5 < Re_f < 40$

$$p_+ = \exp_{p/}\left(\exp_3\left(-\left[\frac{Re_b}{Re_f}\right]^3\right) + \exp_3\left(-\left[\frac{Re_f}{Re_k}\right]^3\right)\left[1 - |\min(0, \cos\psi)|^2\right]\right) \tag{62}$$

$$Re_b = 300\ \exp_{90/300}\left(\cos^2\psi\right) \tag{63}$$

$$Re_k = 5\ \exp_{60/5}\left(1 - |\min(0, \cos\psi)|^2\right) \tag{64}$$

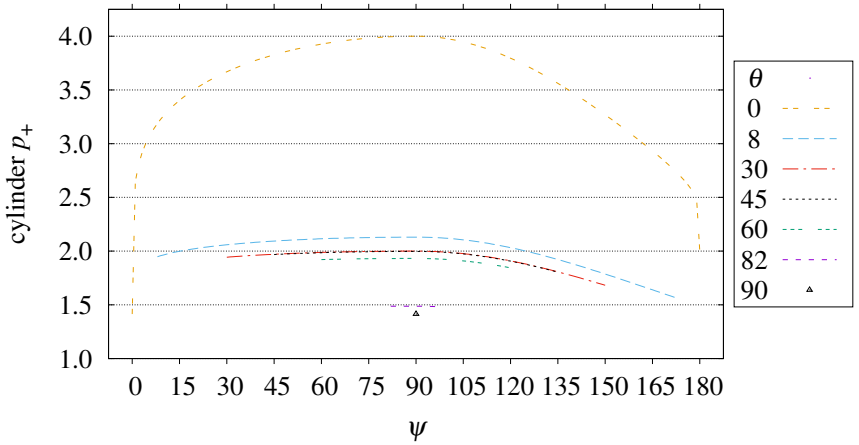

Figure 48 **Cylinder mixed convection** p_+ **versus** Re_f

Plotted in Figure 48, Formulas (62–64) manifest these p constraints and interpolate between them with trigonometric coefficients.

13.6 **Forced Convection Reuptake Kick.** In this section, $Re_F = Re_d$ and Re_N are for the whole disk.

The reuptake coefficients between the rim and faces of a disk are independent of Re_F. Reuptake coefficients between the fixture's tubes and disk may vary with Re_F.

The natural convection reuptake coefficient is the fraction of the disk's $\overline{U_N}$ to be deducted from the total thermal conductance of the disk and tubes. The difficulty of analyzing reuptake for the disk–tube combination is avoided by inferring the disk–tube reuptake coefficient from measurements of natural convection heat transfer. The 1.75% RMSRE between natural reuptake coefficients at θ and $180° - \theta$ in Figure 44, in combination with the practice of positioning the tubes at the disk's leeward edge of forced flow, indicates that reuptake can be calculated based on disk natural convection instead of (more complicated) tubes.

Energy conservation bounds reuptake coefficients between 0 and 1. It is expected that aiding flow will tend to increase the natural reuptake coefficient and opposing flow will tend to decrease it. To meet these constraints, the forced reuptake coefficient will raise the natural reuptake coefficient to a "kick" exponent, $X \geq 0$, calculated from ψ, Re_F, and computed Re_N.

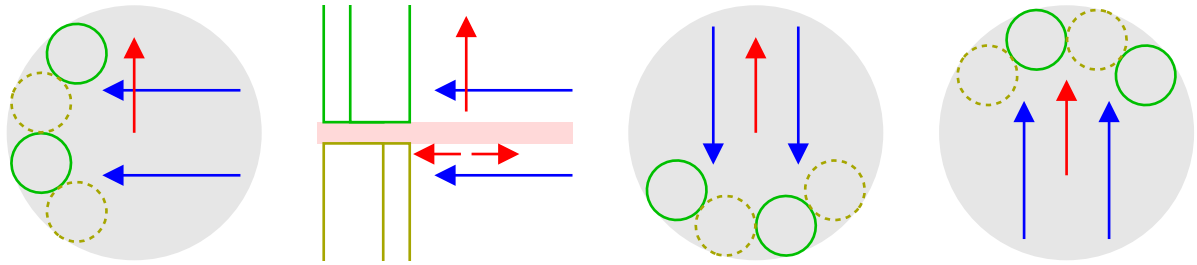

Figure 49 Orientations (a) $\theta = 0, \psi = 90$**; (b)** $\theta = 90, \psi = 90$**; (c)** $\theta = 0, \psi = 180$**; (d)** $\theta = 0, \psi = 0$

Figure 49 has schematic drawings of disks with natural flow as red arrows and forced flow as blue arrows. The green circles represent tubes abutting the near face of the disk; the yellow dashed circles represent tubes abutting the far face of the disk. Figure 49b is an edge view of the horizontal disk with tubes above and below the disk.

Figure 49a is a vertical disk in horizontal forced flow. With little natural convective fluid heating at the bottom of the disk; horizontal forced flow causes little reuptake. Natural convective heating along the upper half of the disk causes upward fluid flow such that the fluid heated by the disk rises above the tubes, escaping reuptake. The "0 90" trace in Figure 50 is a constant 1 in this case.

Figure 49b is a horizontal disk in horizontal forced flow. Forced flow above the disk shifts the natural convective plume towards the upper part of the tubes, which are too far from the disk to significantly reduce heat transfer. Below the disk, still air reuptake is already significant. Horizontal forced flow does not increase it. The "90 90" trace in Figure 51 is a constant 1.

Figure 49c is a vertical disk in downward forced flow. Because the flow directions differ, reuptake is reduced at $60 < Re_F < 1400$ by increased X in the "0 180" trace of Figure 50:

$$X = \exp_4\left(S\,\exp_{1/3}\left(\left[\frac{[\varphi\,Re_F]^3 + {Re_N}^3}{9\,[\varphi\,Re_F\,Re_N]^{3/2}}\right]^4\right)\right) \qquad \cos\psi \leq 0 \tag{65}$$

Figure 49d is a vertical disk in upward forced flow. At $Re_F > 60$, the reuptake factor increases due to reduced X in the "0 0" trace of Figure 50:

$$X = \exp_{1/8}\left(S\left[1 - \exp_{1/3}\left(\frac{9\,{Re_F}^3}{{Re_F}^3 + [\varphi\,Re_N]^3}\right)\right]\right) \qquad \cos\psi \geq 0 \tag{66}$$

When the tubes are not directly above or below the disk center, their interaction potential is reduced. Thus, exponent X is scaled towards 1 by shadow coefficient $0 \leq S \leq 1$, a trigonometric function of ψ:

$$S = \sqrt{|\cos\psi|\,[1 - \sin\psi]} \qquad 0° \leq \psi \leq 180° \tag{67}$$

Coefficient $\varphi = \sqrt[8]{1 - |\sin\psi|}$ reduces the effective Re_F or Re_N to account for the reduced vertical component of wind-speed when forced flow is not vertical.

Figure 50 plots X for vertical disks with ψ at multiples of 30° and at the ψ values tested.
Figure 51 plots X for disks pitched at multiples of 30° and at the θ and ψ values tested.
The differences between Figure 50 and Figure 51 are due to different Re_N values.
Figure 52 plots shadow coefficient S and shift coefficient φ.

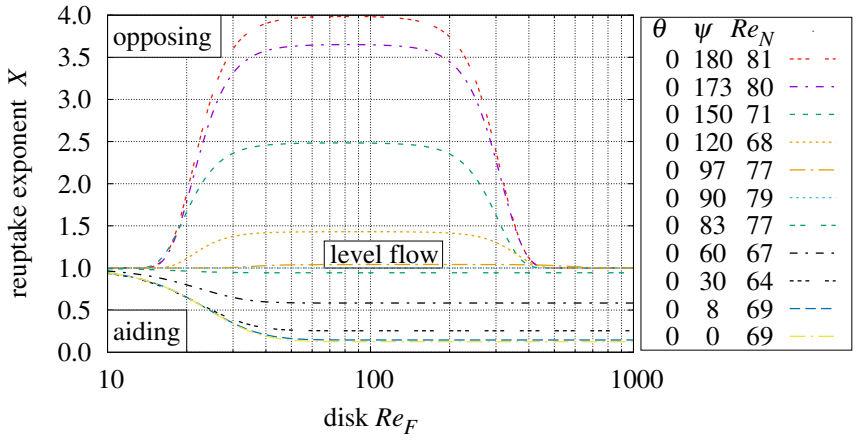

Figure 50 Reuptake exponents of vertical disk

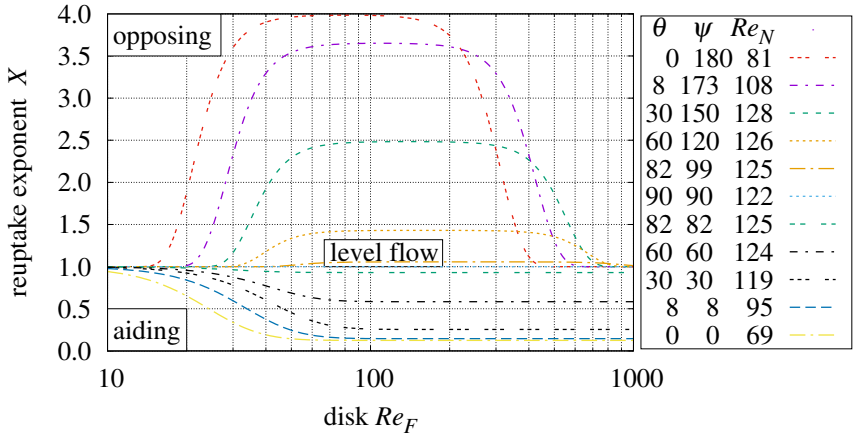

Figure 51 Reuptake exponents of inclined disks

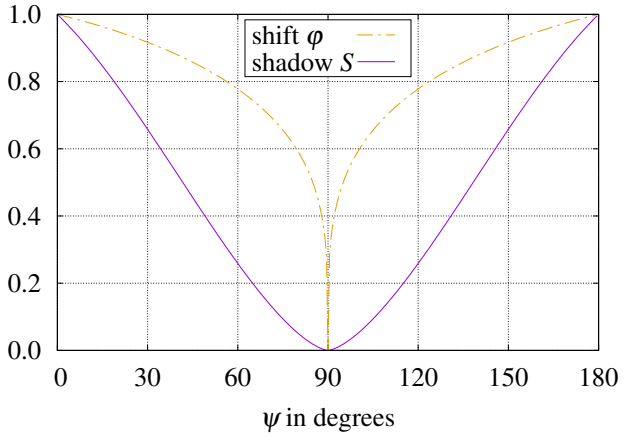

Figure 52 Shadow S and shift φ coefficients

14. References

[1] V Lienhard, John H. Heat Transfer in Flat-Plate Boundary Layers: A Correlation for Laminar, Transitional, and Turbulent Flow. *Journal of Heat Transfer*, 142(6), 04 2020, doi:10.1115/1.4046795. 061805.

[2] Tetsu Fujii and Hideaki Imura. Natural-convection heat transfer from a plate with arbitrary inclination. *International Journal of Heat and Mass Transfer*, 15(4):755–764, 1972, doi:10.1016/0017-9310(72)90118-4.

[3] Stuart W Churchill and Humbert HS Chu. Correlating equations for laminar and turbulent free convection from a vertical plate. *International journal of heat and mass transfer*, 18(11):1323–1329, 1975, doi:10.1016/0017-9310(75)90243-4.

[4] Aubrey Jaffer. Natural convection heat transfer from an isothermal plate. *Thermo*, 3(1):148–175, 2023, doi:10.3390/thermo3010010.

[5] S. W. Churchill and R. Usagi. A general expression for the correlation of rates of transfer and other phenomena. *AIChE Journal*, 18(6):1121–1128, 1972, doi:10.1002/aic.690180606.

[6] Hermann Schlichting. *Boundary-Layer Theory*. McGraw Hill, New Delhi, seventh edition, 2014. Translated by Kestin, J.

[7] C.J. Kobus and G.L. Wedekind. An experimental investigation into forced, natural and combined forced and natural convective heat transfer from stationary isothermal circular disks. *International Journal of Heat and Mass Transfer*, 38(18):3329 – 3339, 1995, doi:10.1016/0017-9310(95)00096-R.

[8] K. Kitamura, A. Mitsuishi, T. Suzuki, and F. Kimura. Fluid flow and heat transfer of natural convection adjacent to upward-facing, rectangular plates of arbitrary aspect ratios. *International Journal of Heat and Mass Transfer*, 89:320–332, 2015, doi:10.1016/j.ijheatmasstransfer.2015.05.075.

[9] T Aihara, Y Yamada, and S Endö. Free convection along the downward-facing surface of a heated horizontal plate. *International Journal of Heat and Mass Transfer*, 15(12):2535 – 2549, 1972, doi:10.1016/0017-9310(72)90145-7.

[10] HT Lin, WS Yu, and CC Chen. Comprehensive correlations for laminar mixed convection on vertical and horizontal flat plates. *Wärme-und Stoffübertragung*, 25(6):353–359, 1990.

[11] N. Ramachandran, B. F. Armaly, and T. S. Chen. Measurements and Predictions of Laminar Mixed Convection Flow Adjacent to a Vertical Surface. *Journal of Heat Transfer*, 107(3):636–641, 08 1985, doi:10.1115/1.3247471.

[12] D L Siebers, R G Schwind, and R J Moffat. Experimental mixed-convection heat transfer from a large, vertical surface in a horizontal flow. Technical report, Sandia National Lab., Livermore, CA (United States), 7 1983.

[13] X. A. Wang. An experimental study of mixed, forced, and free convection heat transfer from a horizontal flat plate to air. *Journal of Heat Transfer*, 104(1):139–144, 1982, doi:10.1115/1.3245040.

[14] C.J Kobus and G.L Wedekind. An empirical correlation for natural convection heat transfer from thin isothermal circular disks at arbitrary angles of inclination. *International Journal of Heat and Mass Transfer*, 45(5):1159–1163, 2002, doi:10.1016/S0017-9310(01)00213-7.

[15] C.J. Kobus and G.L. Wedekind. An experimental investigation into natural convection heat transfer from horizontal isothermal circular disks. *International Journal of Heat and Mass Transfer*, 44(17):3381 – 3384, 2001, doi:10.1016/S0017-9310(00)00330-6.

[16] Aubrey Jaffer and Martin Jaffer. Mixed convection from an isothermal rough plate. *Thermal Science and Engineering*, 8(1), 2025, doi:10.24294/tse9275.

[17] F.P. Incropera, D.P. DeWitt, T.L. Bergman, and A.S. Lavine. *Fundamentals of Heat and Mass Transfer*. Wiley, Hoboken, NJ, USA, 2007.

[18] Aubrey Jaffer. Skin-friction and forced convection from rough and smooth plates. *Thermo*, 3(4):711–775, 2023, doi:10.3390/thermo3040040.

[19] A. Žukauskas and A. Šlančiauskas. *Heat Transfer in Turbulent Fluid Flows*. Hemisphere Publishing Corp, Washington, DC, 1987.

[20] J. H. Lienhard, IV and J. H. Lienhard, V. *A Heat Transfer Textbook*. Phlogiston Press, Cambridge, MA, 5th edition, August 2020. Version 5.10.

[21] J. Kiefer. Sequential minimax search for a maximum. *Proceedings of the American Mathematical Society*, 4(3):502–506, 1953.